J. Fluid Mech. (2024), *vol*. 1000, A46, doi:10.1017/jfm.2024.987

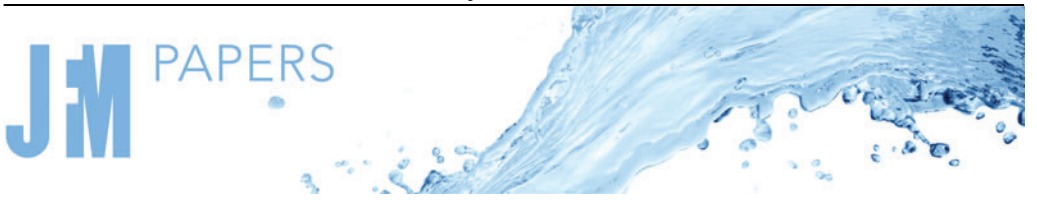

Quasi-linear homogenization for large-inertia laminar transport across permeable membranes

K. Wittkowski[1], **A. Ponte**[2], **P.G. Ledda**[3] **and G.A. Zampogna**[1],†

[1]Laboratory of Fluid Mechanics and Instabilities, École Polytechnique Fédérale de Lausanne, CH-1015 Lausanne, Switzerland

[2]Dipartimento di Ingegneria Civile, Chimica e Ambientale, Università degli Studi di Genova, Via Montallegro 1, 16145 Genova, Italy

[3]Dipartimento di Ingegneria Civile, Ambientale e Architettura, Università degli Studi di Cagliari, Via Marengo 2, 09123 Cagliari, Italy

(Received 22 April 2024; revised 23 August 2024; accepted 7 October 2024)

Porous membranes are thin solid structures that allow the flow to pass through their tiny openings, called pores. Flow inertia may play a significant role in several filtration flows of natural and engineering interest. Here, we develop a predictive macroscopic model to describe solvent and solute flows past thin membranes for non-negligible inertia. We leverage homogenization theory to link the solvent velocity and solute concentration to the jumps of solvent stress and solute flux across the membrane. Within this framework, the membrane acts as a boundary separating two distinct fluid regions. These jump conditions rely on several coefficients, stemming from closure problems at the microscopic pore scale. Two approximations for the advective terms of Navier–Stokes and advection–diffusion equations are introduced to include inertia in the microscopic problem. The approximate inertial terms couple the micro- and macroscopic fields. Here, this coupling is solved numerically using an iterative fixed-point procedure. We compare the resulting models against full-scale simulations, with a good agreement both in terms of averaged values across the membrane and far-field values. Eventually, we develop a strategy based on unsupervised machine learning to improve the computational efficiency of the iterative procedure. The extension of homogenization towards weak-inertia flow configurations as well as the performed data-driven approximation may find application in preliminary analyses as well as optimization procedures towards the design of filtration systems, where inertia effects can be instrumental in broadening the spectrum of permeability and selectivity properties of these filters.

Key words: membranes, porous media

† Email address for correspondence: giuseppe.zampogna@epfl.ch

1. Introduction

Flows across thin permeable structures are encountered in a wide range of engineering situations and nature, see, for example, the stable glide of dandelion seeds thanks to their hairy parachute called pappus (Cummins *et al.* 2018; Ledda *et al.* 2019) and the recirculating patterns inside deep-sea porous sponges, which are beneficial for organisms living within their structure (Falcucci *et al.* 2021, 2024). The filtration properties of these sponges are crucial in defining these patterns and consequently the transport of nutrients.

Related to this, fluidic systems are widely employed for separation and filtration processes (Catarino *et al.* 2019). The flow is usually laminar but, in certain applications, advection may play an important role in the transport of solute (Tripathi *et al.* 2015). Advection effects are quantified through two non-dimensional numbers: the Reynolds number, the ratio between inertial and viscous scales for the fluid flow, and the Péclet number, the ratio between the advective and diffusive scales for the transport of solute in a solvent. In membrane filters for the collection of particles, the Reynolds number can reach values of up to 20 (Yang *et al.* 1999). In hydrogen fuel cells, the Péclet number inside a proton-exchange membrane can be of the order of 10 (Suresh & Jayanti 2016). Microfluidic mixing processes can be enhanced by adding microstructured patterns within the micro-channels (Stroock *et al.* 2002). However, filtration processes do not only involve lab-scale systems. As a matter of fact, nets and harps are attracting interest in harvesting water from fog in arid environments (Park *et al.* 2013; Labbé & Duprat 2019; Moncuquet *et al.* 2022).

Accurately modelling the transport phenomena across porous membranes in the presence of inertial effects thus affects a variety of applications ranging across several length and time scales. Numerical studies concerning the interaction between fluid flows and permeable structures belong to two approaches: full-scale solutions and averaged models. Direct full-scale solutions, such as that reported by Icardi *et al.* (2014), although very accurate, require a non-trivial computational effort from the geometry and mesh generation to the actual numerical solution. This approach rapidly becomes prohibitive for flows at industrial scales or in the case of biological systems with extreme scale separation, e.g. cell membranes, where pores are nanometric and membranes are micrometric (Verkman & Mitra 2000). In addition, full-scale solutions offer sometimes little insight into the general physics governing the processes and they are not scalable in the case of parametric studies or optimization routines. Conversely, simplified models are preferred in some contexts. Some authors have studied analytically the specific case of flow normal to the membrane (Conca 1987; Bourgeat & Marusic-Paloka 1998), while others have developed theories for flow through infinitesimally thin porous membranes and deduced some range of applicability of Stokes' approximation (Tio & Sadhal 1994), or considered simplified pore geometries and arrangements (Jensen, André & Stone 2014*a*). A specific class of simplified flow descriptions consists of averaged models. Early models describe the fluid flow and solute transport across a bulk porous medium with a solvent flow description analogous to Darcy's law (Darcy 1856, see Dagan 1987 for a review). Despite being computationally less expensive, these models converge to the actual fluid flow field only in an average sense and rely on empirical coefficients, like the permeability, difficult to quantify from a theoretical point of view, and thus limit the model's predictive power. Multi-scale techniques such as the volume-averaged method (Whitaker 1996) and homogenization (Hornung 1997) enable a more accurate and predictive description of such flows. In homogenization, the medium properties are the spatially averaged solution of closure problems at the pore-scale level. Zampogna & Gallaire (2020) proposed an

homogenization-based formal approach to predict the permeability properties of thin porous membranes, including the transport of diluted species (Zampogna, Ledda & Gallaire 2022). Ledda *et al.* (2021) showed that this methodology can be used not only for flow analysis, but also for membrane design and optimization. Homogenization thus provides a formal approach for studying and designing porous structures when the flow at the pore scale has negligible inertia. However, at the current state of the art, homogenization cannot handle pore-scale inertial flows since it requires the linearity of the governing pore-scale equations. To overcome this limitation, Zampogna *et al.* (2016) and Luminari, Airiau & Bottaro (2018) proposed an Oseen-like momentum equation to close the pore-scale problem in the case of flows through bulk porous media.

Actual applications in thin membrane flows can significantly benefit from extending beyond the inertia-less regime the modelling and optimization strategies associated with homogenization to better upscale transport and filtration phenomena occurring at the pore scale. In the present work, we generalize the framework proposed by Zampogna *et al.* (2022) for inertial pore-scale flows. In § 2, we present the mathematical derivation of the homogenization procedure. Section 3 presents the solution to the problems we solve at the microscopic level to obtain the effective permeability and diffusivity coefficients, while in § 4, we use these solutions to predict the mean flow behaviour past permeable membranes. We compare our homogeneous model with simulations solved at all scales. In § 5, we improve the computational efficiency of our methodology by introducing a machine learning algorithm to minimize the number of microscopic problems to be solved. In § 6, we discuss our results and future perspectives.

2. Homogenized model and quasi-linear inertial flow extension

We consider the incompressible flow of a Newtonian fluid (so-called solvent) of density ρ and viscosity μ_0 travelling across a thin microstructured porous membrane and transporting a diluted solute of diffusivity D. We introduce the solute concentration $\hat{c}$ and the solvent velocity and pressure fields $\hat{u}_i$, $\hat{p}$. Because of the presence of the diluted solute, the viscosity μ of the solvent–solute ensemble varies linearly with the concentration (Einstein 1906). However, actual variations of viscosity strongly depend on the considered couple solvent–solute. To remain within a general framework, we consider a constant viscosity of the ensemble (Geback & Heintz 2019; Royer 2019), which, for example, can be its average value. The range of dilution in which this hypothesis holds clearly depends on the considered case (cf. for example, the experimental curves by Goldsack & Franchetto 2011), but it allows us to focus on the effect of inertia at the pore scale. The fluid domain and porous structure are depicted in figure 1. Denoting as ℓ and L the pore (micro-scale) and the membrane (macro-scale) length scales, respectively, we define the separation of scales parameter as $\epsilon = \ell/L$. The full-scale problem is governed by the Navier–Stokes equations for the solvent velocity and pressure, as well as by the advection–diffusion equation for the solute concentration,

$$\left.\begin{aligned} \rho(\hat{\partial}_t\hat{u}_i + \hat{u}_j\hat{\partial}_j\hat{u}_i) &= -\hat{\partial}_i\hat{p} + \mu\hat{\partial}^2_{ll}\hat{u}_i, \\ \hat{\partial}_i\hat{u}_i &= 0, \\ \hat{\partial}_t\hat{c} &= -\hat{u}_i\hat{\partial}_i\hat{c} + D\hat{\partial}^2_{ll}\hat{c}, \end{aligned}\right\} \tag{2.1}$$

where the Einstein index notation is adopted. As shown in the following sections, homogenization relies on the following steps (figure 2): (i) define the inner equations

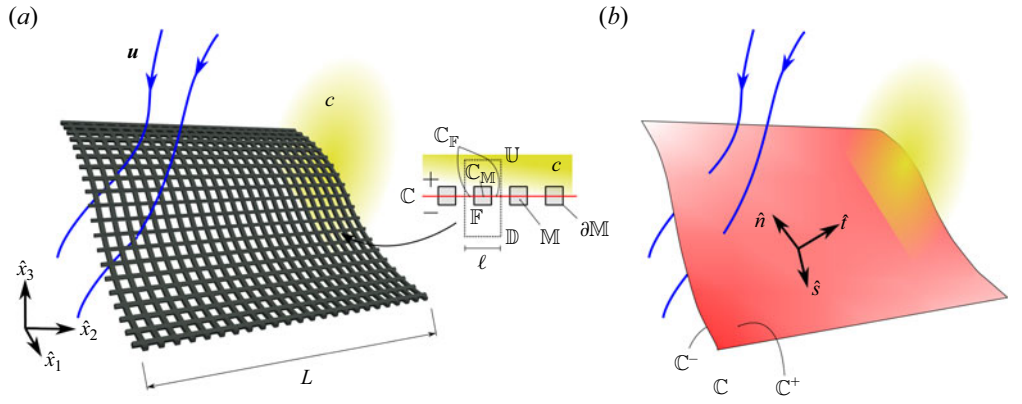

Figure 1. Porous thin membrane. (*a*) Membrane as it appears in the physical world. The fluid flow (blue streamlines) crosses the membrane via its pores and the concentration field (yellow contour) interacts with the membrane surface at the pore scale. (*b*) Purely macroscopic domain, where the membrane is substituted by its mean surface $\mathbb{C}$ and where the details of the pores have been coarse-grained: $\mathbb{C}$ is a fictitious surface, separating two domains, where equivalent boundary conditions are imposed to reproduce the average effect of the membrane on the fluid flow and concentration fields.

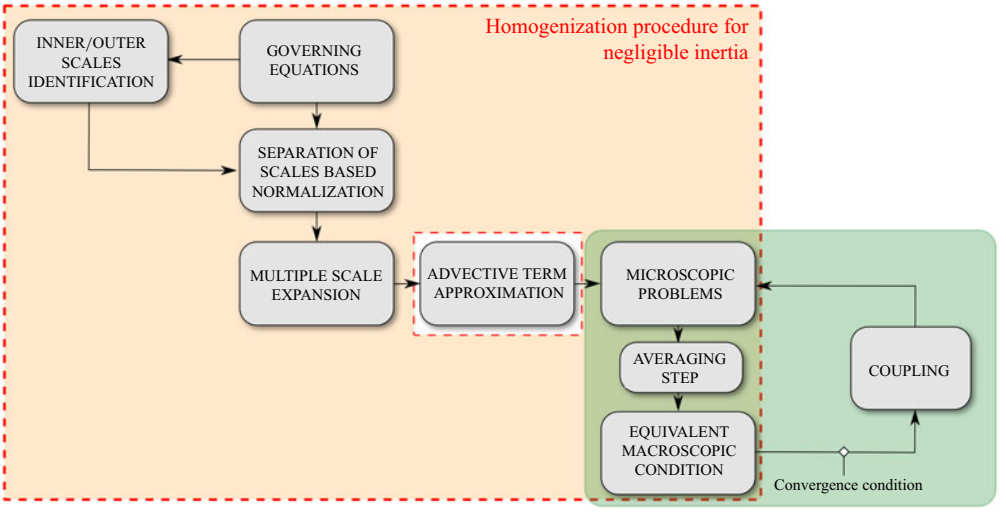

Figure 2. Diagram of the procedure used to deduce the macroscopic model. The green box highlights the novel iterative part of the procedure.

and normalization, which apply at the pore scale; (ii) define the outer equations and normalizations, which apply far from the membrane; (iii) match the inner and outer domains; (iv) solve the inner (microscopic) problem; (v) average the inner solution and deduce the macroscopic condition.

2.1. *The inner problem*

We refer to the domain $\mathbb{F}$ in figure 1(*a*) as the microscopic domain, in opposition to the outer, macroscopic domain, formed by the fluid region far from the membrane (figure 1*b*).

In the inner domain, we employ the following scaling:

$$\hat{p} = \Delta\mathcal{P}p = \frac{\mu\mathcal{U}}{\ell}p, \quad \hat{u} = \mathcal{U}u, \quad \hat{\mathrm{t}} = T\mathrm{t} = \frac{\ell}{\mathcal{U}}\mathrm{t}, \quad \hat{c} = Cc, \tag{2.2a–d}$$

where $\Delta\mathcal{P}, \mathcal{U}, T$ and C are the scales of pressure difference, velocity, time and concentration at the pore level, respectively. The equations governing the physics within the microscopic elementary cell, $\mathbb{F}$, are

$$\left.\begin{aligned} Re_\ell(\partial_\mathrm{t}u_i + u_j\partial_j u_i) &= -\partial_i p + \partial^2_{ll}u_i, \\ \partial_i u_i &= 0, \\ Pe_\ell\partial_\mathrm{t}c &= -Pe_\ell u_i\partial_i c + \partial^2_{ll}c, \end{aligned}\right\} \tag{2.3}$$

where $Pe_\ell = \mathcal{U}\ell/D$ and $Re_\ell = \mathcal{U}\ell/\nu$ are the Péclet and Reynolds numbers referring to the microscopic length ℓ, respectively. The flow is assumed to be periodic along the tangential-to-the-membrane directions. No-slip ($u_i = 0$) and chemostat-like ($c = 0$) boundary conditions are imposed on the fluid–solid interface $\partial\mathbb{M}$. These Dirichlet boundary conditions are contained in the more general set of Robin boundary conditions presented by Zampogna *et al.* (2022). The inner flow is assumed continuous with the outer flow, in terms of velocity, stress, concentration and solute flux at the upward $\mathbb{U}$ and downward $\mathbb{D}$ sides (cf. figure 1) of the microscopic domain.

2.2. *The outer problem*

In the macroscopic domain, we employ the following non-dimensionalization to scale the equations:

$$\hat{p} = \Delta\mathcal{P}^{\mathbb{O}}p^{\mathbb{O}} = \rho{\mathcal{U}^{\mathbb{O}}}^2 p^{\mathbb{O}}, \quad \hat{u} = \mathcal{U}^{\mathbb{O}}u^{\mathbb{O}}, \quad \hat{\mathrm{t}} = T^{\mathbb{O}}\mathrm{t}^{\mathbb{O}} = \frac{L}{\mathcal{U}^{\mathbb{O}}}\mathrm{t}^{\mathbb{O}}, \quad \hat{c} = C^{\mathbb{O}}c^{\mathbb{O}}. \tag{2.4a–d}$$

The governing equations of the outer problem are

$$\left.\begin{aligned} \partial_\mathrm{t}u_i^{\mathbb{O}} + u_j^{\mathbb{O}}\partial_j u_i^{\mathbb{O}} &= -\partial_i p^{\mathbb{O}} + \frac{1}{Re_L}\partial^2_{ll}u_i^{\mathbb{O}}, \\ \partial_i u_i^{\mathbb{O}} &= 0, \\ Pe_L\partial_\mathrm{t}c^{\mathbb{O}} &= -Pe_L u_i^{\mathbb{O}}\partial_i c^{\mathbb{O}} + \partial^2_{ll}c^{\mathbb{O}}, \end{aligned}\right\} \tag{2.5}$$

where $Pe_L = \mathcal{U}^{\mathbb{O}}L/D$ and $Re_L = \mathcal{U}^{\mathbb{O}}L/\nu$.

2.3. *Matching the inner and outer domains*

To observe inertial effects at the pore scale, we require at least $Re_L \sim Pe_L \sim 1/\epsilon$ and $Re_\ell \sim Pe_\ell \sim 1$, and thus we assume $\mathcal{U} \sim \mathcal{U}^{\mathbb{O}}$. Consequently, the ratio of microscopic and macroscopic time scales reads

$$\frac{T}{T^{\mathbb{O}}} = \frac{\ell}{\mathcal{U}}\frac{\mathcal{U}^{\mathbb{O}}}{L} = \epsilon\frac{\mathcal{U}^{\mathbb{O}}}{\mathcal{U}} \sim \epsilon. \tag{2.6}$$

Equation (2.6) suggests that variations at the micro-scale occur in a much shorter time compared with the characteristic time variations at the macro-scale, and thus the pore-scale

problem can be considered steady if no unsteadiness is triggered at the micro-scale,

$$\left.\begin{aligned} Re_\ell u_j \partial_j u_i &= -\partial_i p + \partial^2_{ll} u_i, \\ \partial_i u_i &= 0, \\ -Pe_\ell u_i \partial_i c &+ \partial^2_{ll} c = 0. \end{aligned}\right\} \tag{2.7}$$

On the upward $\mathbb{U}$ and downward $\mathbb{D}$ sides of $\mathbb{F}$, the dimensional outer and inner fluid flow and concentration fields match, i.e.

$$\hat{\Sigma}_{ij} n_j = \hat{\Sigma}^{\mathbb{O}}_{ij} n_j \Rightarrow [-\hat{p}\delta_{ij} + \mu(\hat{\partial}_i \hat{u}_j + \hat{\partial}_j \hat{u}_i)] n_j = [-\hat{p}^{\mathbb{O}}\delta_{ij} + \mu(\hat{\partial}_i \hat{u}^{\mathbb{O}}_j + \hat{\partial}_j \hat{u}^{\mathbb{O}}_i)] n_j$$

$$\Rightarrow \left[-\frac{\mu\mathcal{U}}{\ell} p\delta_{ij} + \frac{\mu\mathcal{U}}{\ell}(\partial_i u_j + \partial_j u_i)\right] n_j = \left[-\rho\mathcal{U}^{\mathbb{O}2} p^{\mathbb{O}}\delta_{ij} + \frac{\mu\mathcal{U}^{\mathbb{O}}}{L}(\partial_i u^{\mathbb{O}}_j + \partial_j u^{\mathbb{O}}_i)\right] n_j$$

$$\Rightarrow \Sigma_{ij} n_j = \epsilon\, Re_L \frac{\mathcal{U}^{\mathbb{O}}}{\mathcal{U}} \Sigma^{\mathbb{O}}_{ij} n_j, \tag{2.8a}$$

$$\hat{F}_i n_i = \hat{F}^{\mathbb{O}}_i n_i \Rightarrow [\hat{u}_i \hat{c} - D\hat{\partial}_i \hat{c}] n_i = [\hat{u}^{\mathbb{O}}_i \hat{c}^{\mathbb{O}} - D\hat{\partial}_i \hat{c}^{\mathbb{O}}] n_i$$

$$\Rightarrow \left[\mathcal{U} C u_i c - D\frac{C}{\ell}\partial_i c\right] n_i = \left[\mathcal{U}^{\mathbb{O}} C^{\mathbb{O}} u^{\mathbb{O}}_i c^{\mathbb{O}} - D\frac{C^{\mathbb{O}}}{L}\partial_i c^{\mathbb{O}}\right] n_i$$

$$\Rightarrow F_i n_i = \epsilon \frac{C^{\mathbb{O}}}{C} F^{\mathbb{O}}_i n_i, \tag{2.8b}$$

$$u = \frac{\mathcal{U}^{\mathbb{O}}}{\mathcal{U}} u^{\mathbb{O}}, \quad c = \frac{C^{\mathbb{O}}}{C} c^{\mathbb{O}}, \tag{2.8c,d}$$

where $\Sigma_{jk} = -p\delta_{jk} + (\partial_j u_k + \partial_k u_j)$, $\Sigma^{\mathbb{O}}_{jk} = -p^{\mathbb{O}}\delta_{jk} + \frac{1}{Re_L}(\partial_j u^{\mathbb{O}}_k + \partial_k u^{\mathbb{O}}_j)$, $F_j = Pe_\ell u_i c - \partial_i c$ and $F^{\mathbb{O}}_j = Pe_L u^{\mathbb{O}}_i c^{\mathbb{O}} - \partial_i c^{\mathbb{O}}$ are the fluid stresses and solute fluxes in the inner and outer domains, respectively.

2.4. *Solving the inner problem*

To apply homogenization to the problem in (2.7), the Stokes approximation assumes $Re_\ell \sim Pe_\ell \sim \epsilon$ (Zampogna *et al.* 2022). In this paper, we introduce finite Péclet and Reynolds numbers at the pore scale, i.e. $Re_\ell \sim 1$ and $Pe_\ell \sim 1$. Consequently, the problem in (2.7) is a set of nonlinear partial differential equations. Exploiting the separation of scales, we perform the following asymptotic expansion:

$$\left.\begin{aligned} x_i &= x_i + \epsilon X_i, \quad \partial_i = \partial_i + \epsilon \partial_I, \\ (u_i, p, c) &= (u^{(0)}_i, p^{(0)}, c^{(0)}) + \epsilon(u^{(1)}_i, p^{(1)}, c^{(1)}) + \mathcal{O}(\epsilon^2). \end{aligned}\right\} \tag{2.9}$$

Substituting (2.9) into (2.7), we obtain the leading order equation,

$$\left.\begin{aligned} Re_\ell u_j^{(0)}\partial_j u_i^{(0)} &= -\partial_i p^{(0)} + \partial_{ll}^2 u_i^{(0)},\\ \partial_i u_i^{(0)} &= 0,\\ -Pe_\ell u_i^{(0)}\partial_i c^{(0)} + \partial_{ll}^2 c^{(0)} &= 0,\\ \Sigma_{ij}^{(0)} n_j = \Sigma_{ij}^{\mathbb{O}} n_j \quad &\text{on } \mathbb{U}, \mathbb{D},\\ u_i^{(0)} = 0 \quad &\text{on } \partial\mathbb{M},\\ u_i^{(0)}, p^{(0)} \quad &\text{periodic along } \boldsymbol{t}, \boldsymbol{s}. \end{aligned}\right\} \tag{2.10}$$

To write the solution of (2.10) as a linear combination of the boundary fluxes, we introduce the closure advective velocity U_j such that

$$\left.\begin{aligned} Re_\ell U_j\partial_j u_i^{(0)} &= -\partial_i p^{(0)} + \partial_{ll}^2 u_i^{(0)},\\ \partial_i u_i^{(0)} &= 0,\\ -Pe_\ell U_j\partial_j c^{(0)} + \partial_{ll}^2 c^{(0)} &= 0,\\ \Sigma_{ij}^{(0)} n_j = \Sigma_{ij}^{\mathbb{O}} n_j \quad &\text{on } \mathbb{U}, \mathbb{D},\\ u_i^{(0)} = 0 \quad &\text{on } \partial\mathbb{M},\\ u_i^{(0)}, p^{(0)} \quad &\text{periodic along } \boldsymbol{t}, \boldsymbol{s}. \end{aligned}\right\} \tag{2.11}$$

The term U_j needs to be specified to close (2.11). However, we refer to § 2.6 for the closure of U_j. The solution of (2.11) can be formally written as a linear combination of the boundary fluxes,

$$\left.\begin{aligned} u_i^{(0)} &= \epsilon Re_L \frac{\mathcal{U}^{\mathbb{O}}}{\mathcal{U}}(M_{ij}\Sigma_{jk}^{\mathbb{O},\mathbb{U}} n_k + N_{ij}\Sigma_{jk}^{\mathbb{O},\mathbb{D}} n_k),\\ p^{(0)} &= \epsilon Re_L \frac{\mathcal{U}^{\mathbb{O}}}{\mathcal{U}}(Q_j\Sigma_{jk}^{\mathbb{O},\mathbb{U}} n_k + R_j\Sigma_{jk}^{\mathbb{O},\mathbb{D}} n_k),\\ c^{(0)} &= \epsilon \frac{C^{\mathcal{O}}}{C}(TF_j^{\mathbb{O},\mathbb{U}} n_j + SF_j^{\mathbb{O},\mathbb{D}} n_j). \end{aligned}\right\} \tag{2.12}$$

Substituting (2.12) into (2.11), we obtain the set of solvability conditions:

$$\left.\begin{aligned} Re_\ell U_m\partial_m M_{ij} &= -\partial_i Q_j + \partial_{ll}^2 M_{ij} \quad \text{in } \mathbb{F},\\ \partial_i M_{ij} &= 0 \quad \text{in } \mathbb{F},\\ \Sigma_{pq}(M_{\cdot j}, Q_j) n_q &= \delta_{jp} n_q \quad \text{on } \mathbb{U},\\ \Sigma_{pq}(M_{\cdot j}, Q_j) n_q &= 0 \quad \text{on } \mathbb{D},\\ M_{ij} &= 0 \quad \text{on } \partial\mathbb{M},\\ M_{ij}, Q_j \quad &\text{periodic along } \boldsymbol{t}, \boldsymbol{s}, \end{aligned}\right\} \tag{2.13a}$$

$$\left.\begin{aligned} Re_\ell U_m \partial_m N_{ij} &= -\partial_i R_j + \partial^2_{ll} N_{ij} \quad \text{in } \mathbb{F}, \\ \partial_i N_{ij} &= 0 \quad \text{in } \mathbb{F}, \\ \Sigma_{pq}(N_{\cdot j}, R_j) n_q &= 0 \quad \text{on } \mathbb{U}, \\ \Sigma_{pq}(N_{\cdot j}, R_j) n_q &= \delta_{jp} n_q \quad \text{on } \mathbb{D}, \\ N_{ij} &= 0 \quad \text{on } \partial\mathbb{M}, \\ N_{ij}, R_j &\quad \text{periodic along } \boldsymbol{t}, \boldsymbol{s}, \end{aligned}\right\} \tag{2.13b}$$

$$\left.\begin{aligned} Pe_\ell U_j \partial_j T - \partial^2_{ll} T &= 0 \quad \text{in } \mathbb{F}, \\ (Pe_\ell U_j T - \partial_j T) n_j &= 1 \quad \text{on } \mathbb{U}, \\ (Pe_\ell U_j T - \partial_j T) n_j &= 0 \quad \text{on } \mathbb{D}, \\ T &= 0 \quad \text{on } \partial\mathbb{M}, \\ T &\quad \text{periodic along } \boldsymbol{t}, \boldsymbol{s}, \end{aligned}\right\} \quad \left.\begin{aligned} Pe_\ell U_j \partial_j S - \partial^2_{ll} S &= 0 \quad \text{in } \mathbb{F}, \\ (Pe_\ell U_j S - \partial_j S) n_j &= 0 \quad \text{on } \mathbb{U}, \\ (Pe_\ell U_j S - \partial_j S) n_j &= 1 \quad \text{on } \mathbb{D}, \\ S &= 0 \quad \text{on } \partial\mathbb{M}, \\ S &\quad \text{periodic along } \boldsymbol{t}, \boldsymbol{s}, \end{aligned}\right\} \tag{2.13c,d}$$

where $\Sigma_{pq}(M_{\cdot j}, Q_j) = -Q_j \delta_{pq} + (\partial_q M_{pj} + \partial_p M_{qj})$ and similarly for N_{ij}, R_j. Since Σ_{pq} contain the quantities Q_j, R_j, no additional boundary condition is needed for the closing of these equations. The first (second) problem in (2.13) represents the pore-level solvent transport in response to normal and tangential unitary stresses on the upward side $\mathbb{U}$ (downward side $\mathbb{D}$) of the membrane. Conversely, the third (fourth) problem represents the pore-level solute transport across the membrane caused by a unitary solute flux entering the upward side $\mathbb{U}$ (downward side $\mathbb{D}$) of the membrane. We notice that by integrating in $\mathbb{F}$ the last two problems in (2.13) and applying the divergence theorem, we obtain an integral balance of solute fluxes which states that the solute flux entering from the $\mathbb{U}$ or $\mathbb{D}$ side is removed from the domain at the boundary $\partial\mathbb{M}$ because of its boundary condition. The solvability conditions in (2.13) slightly differ from those introduced by Zampogna *et al.* (2022) because of the presence of the advective term. In the case of flows on rough, impermeable surfaces, Bottaro (2019) and Lācis *et al.* (2020) showed that the systems in (2.13) are equivalent to the following set of equations:

$$\left.\begin{aligned} Re_\ell U_m \partial_m M_{ij} &= -\partial_i Q_j + \partial^2_{ll} M_{ij} + \delta_{\mathbb{C}} \delta_{ij}, \\ \partial_i M_{ij} &= 0, \\ \Sigma_{pq}(M_{\cdot j}, Q_j) n_q &= 0 \quad \text{on } \mathbb{U}, \mathbb{D}, \\ M_{ij} &= 0 \quad \text{on } \partial\mathbb{M}, \\ M_{ij}, Q_j &\quad \text{periodic along } \boldsymbol{t}, \boldsymbol{s}, \end{aligned}\right\} \tag{2.14a}$$

$$\left.\begin{aligned} Re_\ell U_m \partial_m N_{ij} &= -\partial_i R_j + \partial^2_{ll} N_{ij} - \delta_{\mathbb{C}} \delta_{ij}, \\ \partial_i N_{ij} &= 0, \\ \Sigma_{pq}(N_{\cdot j}, R_j) n_q &= 0 \quad \text{on } \mathbb{U}, \mathbb{D}, \\ N_{ij} &= 0 \quad \text{on } \partial\mathbb{M}, \\ N_{ij}, R_j &\quad \text{periodic along } \boldsymbol{t}, \boldsymbol{s}, \end{aligned}\right\} \tag{2.14b}$$

$$\left.\begin{array}{c} Pe_\ell U_j \partial_j T - \partial^2_{ll} T + \delta_{\mathbb{C}} = 0 \quad \text{in } \mathbb{F}, \\ (Pe_\ell U_j T - \partial_j T) n_j = 0 \quad \text{on } \mathbb{U}, \mathbb{D}, \\ T = 0 \quad \text{on } \partial\mathbb{M}, \\ T \quad \text{periodic along } \boldsymbol{t}, \boldsymbol{s}, \end{array}\right\} \tag{2.14c}$$

$$\left.\begin{array}{c} Pe_\ell U_j \partial_j S - \partial^2_{ll} S - \delta_{\mathbb{C}} = 0 \quad \text{in } \mathbb{F}, \\ (Pe_\ell U_j S - \partial_j S) n_j = 0 \quad \text{on } \mathbb{U}, \mathbb{D}, \\ S = 0 \quad \text{on } \partial\mathbb{M}, \\ S \quad \text{periodic along } \boldsymbol{t}, \boldsymbol{s}, \end{array}\right\} \tag{2.14d}$$

where $\delta_{\mathbb{C}}$ is a Dirac impulse centred in $x_{\mathbb{C}}$. The physical significance of the problems in (2.13) and (2.14) is similar, but here the forcing is represented by a unitary volume source appearing in the momentum and advection–diffusion equations. The quantities $M_{ij}, N_{ij}, Q_i, R_i, T$ and S depend parametrically on the closure advective velocity U_j. In the present paper, we adopt the formulation in (2.14) to compute the microscopic solution.

2.5. *Averaging step and macroscopic condition*

To upscale the microscopic solutions, we introduce the following averages at both the upstream and downstream sides of the membrane:

$$\bar{M}_{ij} = \frac{1}{|\mathbb{U}|}\int_{\mathbb{U}} M_{ij}\,\mathrm{d}x_t\,\mathrm{d}x_s, \quad \bar{N}_{ij} = \frac{1}{|\mathbb{D}|}\int_{\mathbb{D}} N_{ij}\,\mathrm{d}x_t\,\mathrm{d}x_s. \tag{2.15a,b}$$

We clarify the physical significance of the $\bar{M}_{ij}$ tensors in a two-dimensional domain: $\bar{M}_{nn}$ and $\bar{M}_{tn}$ represent the ability of the fluid to move along the positive normal and tangential directions as a consequence of a normal unitary forcing. Instead, $\bar{M}_{nt}$ and $\bar{M}_{tt}$ represent the ability of the fluid to move along the positive normal and tangential directions as a consequence of a tangential unitary forcing. The same applies for $\bar{N}_{ij}$, with negative normal and tangential directions. Thus, $\bar{M}_{nn}$ and $\bar{M}_{tt}$ can be interpreted as a permeability and a slip coefficient, respectively. The same average definitions apply to the quantities T and S,

$$\bar{T} = \frac{1}{|\mathbb{U}|}\int_{\mathbb{U}} T\,\mathrm{d}x_t\,\mathrm{d}x_s, \quad \bar{S} = \frac{1}{|\mathbb{D}|}\int_{\mathbb{D}} S\,\mathrm{d}x_t\,\mathrm{d}x_s. \tag{2.16a,b}$$

These quantities can be interpreted as effective solute diffusivities relative to a unitary solute flux in the positive ($\bar{T}$) and negative ($\bar{S}$) directions. Quantities $\boldsymbol{M}, \boldsymbol{N}, T, S$ are not solely properties of the geometry (as in the inertia-less case of Zampogna & Gallaire 2020), but also of the fluid flow since they depend on the closure advective velocity.

Applying averages ((2.15), (2.16)) to (2.12), the following macroscopic boundary conditions are obtained:

$$\left.\begin{array}{c} \bar{u}^{\mathbb{O}}_i = \epsilon Re_L(\bar{M}_{ij}\Sigma^{\mathbb{O},\mathbb{U}}_{jk} n_k + \bar{N}_{ij}\Sigma^{\mathbb{O},\mathbb{D}}_{jk} n_k), \\ \bar{c}^{\mathbb{O}} = \epsilon(\bar{T}F^{\mathbb{O},\mathbb{U}}_j n_j + \bar{S}F^{\mathbb{O},\mathbb{D}}_j n_j). \end{array}\right\} \tag{2.17}$$

We specify that (2.17) is obtained from (2.12) by re-normalizing with the outer scales in (2.8).

2.6. *The closure advective velocity*

The solution to (2.14) lies in the closure advective velocity that gives rise to an inertia-driven coupling between the macroscopic and microscopic flows. Two different definitions have been considered in the present work:

(i) a constant advective velocity in the microscopic cell

$$U_i = \bar{u}_i^{\mathbb{O}}, \tag{2.18}$$

which leads to an Oseen-like equation (constant advection closure). This approach has already been proposed in the volume-averaged and homogenization frameworks by other authors for the flow over rough surfaces (Bottaro 2019; Zampogna, Magnaudet & Bottaro 2019);

(ii) a spatially dependent closure advective velocity, reconstructed from the outer stresses (variable advection closure),

$$U_i = \epsilon Re_L (M_{ij} \Sigma_{jk}^{\mathbb{O},\mathbb{U}} n_k + N_{ij} \Sigma_{jk}^{\mathbb{O},\mathbb{D}} n_k). \tag{2.19}$$

A similar approach has been proposed for the flow in bulk porous media (Valdés-Parada & Lasseux 2021; Sánchez-Vargas *et al.* 2023).

The equations for M_{ij}, Q_j, T in the microscopic problems thus become:

(i) for the constant advection closure approach in (2.18):

$$\left.\begin{gathered} \epsilon Re_L \frac{\mathcal{U}}{\mathcal{U}^{\mathbb{O}}} \bar{u}_m^{\mathbb{O}} \partial_m M_{ij} = -\partial_i Q_j + \partial_{ll}^2 M_{ij} + \delta_{\mathbb{C}} \delta_{ij}, \\ \partial_i M_{ij} = 0, \\ \Sigma_{pq}(M_{.j}, Q_j) n_q = 0 \quad \text{on } \mathbb{U}, \mathbb{D}, \\ M_{ij} = 0 \quad \text{on } \partial\mathbb{M}, \\ M_{ij}, Q_j \quad \text{periodic along } \boldsymbol{t}, \boldsymbol{s}; \end{gathered}\right\} \tag{2.20a}$$

$$\left.\begin{gathered} \epsilon Re_L \frac{\mathcal{U}}{\mathcal{U}^{\mathbb{O}}} \bar{u}_m^{\mathbb{O}} \partial_m N_{ij} = -\partial_i R_j + \partial_{ll}^2 N_{ij} - \delta_{\mathbb{C}} \delta_{ij}, \\ \partial_i N_{ij} = 0, \\ \Sigma_{pq}(N_{.j}, R_j) n_q = 0 \quad \text{on } \mathbb{U}, \mathbb{D}, \\ N_{ij} = 0 \quad \text{on } \partial\mathbb{M}, \\ N_{ij}, R_j \quad \text{periodic along } \boldsymbol{t}, \boldsymbol{s}; \end{gathered}\right\} \tag{2.20b}$$

$$\left.\begin{gathered} \epsilon Pe_L \frac{\mathcal{U}}{\mathcal{U}^{\mathbb{O}}} \bar{u}_i^{\mathbb{O}} \partial_j T - \partial_{ll}^2 T + \delta_{\mathbb{C}} = 0, \\ (\epsilon Pe_L \bar{u}_i^{\mathbb{O}} T - \partial_j T) n_j = 0 \quad \text{on } \mathbb{U}, \mathbb{D}, \\ T = 0 \quad \text{on } \partial\mathbb{M}, \\ T \quad \text{periodic along } \boldsymbol{t}, \boldsymbol{s}; \end{gathered}\right\} \tag{2.20c}$$

$$\left.\begin{gathered}\epsilon Pe_L \frac{\mathcal{U}}{\mathcal{U}^{\mathbb{O}}}\bar{u}_i^{\mathbb{O}}\partial_j S - \partial_{ll}^2 S - \delta_{\mathbb{C}} = 0,\\ (\epsilon Pe_L \bar{u}_i^{\mathbb{O}} S - \partial_j S)n_j = 0 \quad \text{on } \mathbb{U}, \mathbb{D},\\ S = 0 \quad \text{on } \partial\mathbb{M},\\ S \quad \text{periodic along } \boldsymbol{t}, \boldsymbol{s};\end{gathered}\right\} \tag{2.20d}$$

(ii) for the variable advection closure approach in (2.19):

$$\left.\begin{gathered}\epsilon^2 Re_L^2 \frac{\mathcal{U}}{\mathcal{U}^{\mathbb{O}}}(M_{mn}\Sigma_{nl}^{\mathbb{O},\mathbb{U}} n_l + N_{mn}\Sigma_{nl}^{\mathbb{O},\mathbb{D}} n_l)\partial_m M_{ij} = -\partial_i Q_j + \partial_{ll}^2 M_{ij} + \delta_{\mathbb{C}}\delta_{ij},\\ \partial_i M_{ij} = 0,\\ \Sigma_{pq}(M_{\cdot j}, Q_j)n_q = 0 \quad \text{on } \mathbb{U}, \mathbb{D},\\ M_{ij} = 0 \quad \text{on } \partial\mathbb{M},\\ M_{ij}, Q_{jk} \quad \text{periodic along } \boldsymbol{t}, \boldsymbol{s};\end{gathered}\right\} \tag{2.21a}$$

$$\left.\begin{gathered}\epsilon^2 Re_L^2 \frac{\mathcal{U}}{\mathcal{U}^{\mathbb{O}}}(M_{mn}\Sigma_{nl}^{\mathbb{O},\mathbb{U}} n_l + N_{mn}\Sigma_{nl}^{\mathbb{O},\mathbb{D}} n_l)\partial_m N_{ij} = -\partial_i R_j + \partial_{ll}^2 N_{ij} - \delta_{\mathbb{C}}\delta_{ij},\\ \partial_i N_{ij} = 0,\\ \Sigma_{pq}(N_{\cdot j}, R_j)n_q = 0 \quad \text{on } \mathbb{U}, \mathbb{D},\\ N_{ij} = 0 \quad \text{on } \partial\mathbb{M},\\ N_{ij}, R_j \quad \text{periodic along } \boldsymbol{t}, \boldsymbol{s};\end{gathered}\right\} \tag{2.21b}$$

$$\left.\begin{gathered}\epsilon^2 Pe_L \frac{\mathcal{U}}{\mathcal{U}^{\mathbb{O}}}(M_{mn}\Sigma_{nl}^{\mathbb{O},\mathbb{U}} n_l + N_{mn}\Sigma_{nl}^{\mathbb{O},\mathbb{D}} n_l)\partial_j T - \partial_{ll}^2 T + \delta_{\mathbb{C}} = 0,\\ (\epsilon^2 Pe_L(M_{mn}\Sigma_{nl}^{\mathbb{O},\mathbb{U}} n_l + N_{mn}\Sigma_{nl}^{\mathbb{O},\mathbb{D}} n_l)T - \partial_j T)n_j = 0 \quad \text{on } \mathbb{U}, \mathbb{D},\\ T = 0 \quad \text{on } \partial\mathbb{M},\\ T \quad \text{periodic along } \boldsymbol{t}, \boldsymbol{s};\end{gathered}\right\} \tag{2.21c}$$

$$\left.\begin{gathered}\epsilon^2 Pe_L \frac{\mathcal{U}}{\mathcal{U}^{\mathbb{O}}}(M_{mn}\Sigma_{nl}^{\mathbb{O},\mathbb{U}} n_l + N_{mn}\Sigma_{nl}^{\mathbb{O},\mathbb{D}} n_l)\partial_j S - \partial_{ll}^2 S - \delta_{\mathbb{C}} = 0,\\ (\epsilon^2 Pe_L(M_{mn}\Sigma_{nl}^{\mathbb{O},\mathbb{U}} n_l + N_{mn}\Sigma_{nl}^{\mathbb{O},\mathbb{D}} n_l)S - \partial_j S)n_j = 0 \quad \text{on } \mathbb{U}, \mathbb{D},\\ S = 0 \quad \text{on } \partial\mathbb{M},\\ S \quad \text{periodic along } \boldsymbol{t}, \boldsymbol{s}.\end{gathered}\right\} \tag{2.21d}$$

The tensors and scalars used in (2.17) are found either by solving (2.20) or (2.21). A computational iterative strategy to interface the macroscopic fields with the microscopic problems is required.

3. Solution of the microscopic problems

We investigate the influence of the closure advective velocity on the microscopic fields M_{ij}, N_{ij}, T and S, in the constant and variable advection closure cases. We introduce the porosity $\theta = |\mathbb{C}_{\mathbb{F}}|/|\mathbb{C}_{\mathbb{F}} \cup \mathbb{C}_{\mathbb{M}}|$ as the fluid-to-total ratio at the membrane centreline $\mathbb{C}$

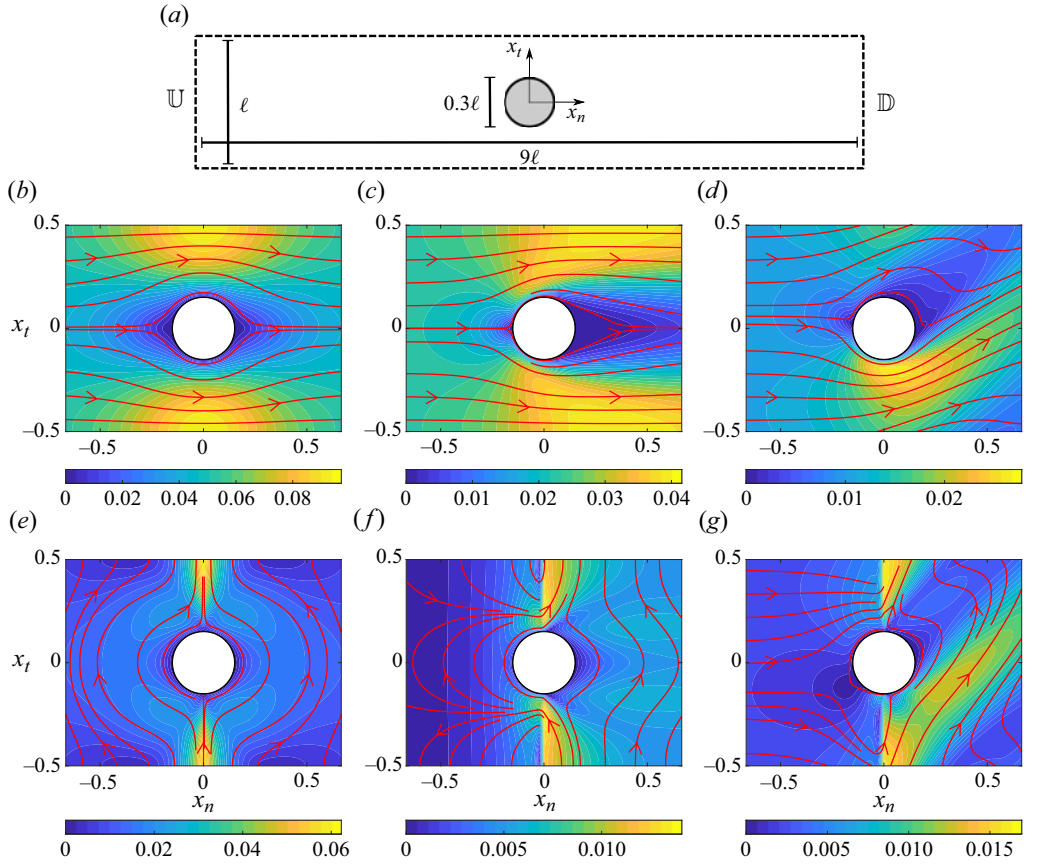

Figure 3. Flow fields within the microscopic domain with different advective velocities $\breve{u}_i$ obtained by solving the first two problems in the constant advection closure in (2.20) around a circular solid inclusion. (*a*) Microscopic domain. (*b–g*) Magnitude contours and streamlines (red) of (M_{nn}, M_{tn}) for (*b*) $\breve{u}_n = 0, \breve{u}_t = 0$, (*c*) $\breve{u}_n = 50, \breve{u}_t = 0$, (*d*) $\breve{u}_n = 50, \breve{u}_t = 50$. Magnitude contours and streamlines of the tensors (M_{nt}, M_{tt}) for (*e*) $\breve{u}_n = 0, \breve{u}_t = 0$, (*f*) $\breve{u}_n = 50, \breve{u}_t = 0$, (*g*) $\breve{u}_n = 50, \breve{u}_t = 50$.

(cf. figure 1*a*). As a benchmark, we consider a circular inclusion of porosity $\theta = 0.7$ (cf. figure 3*a*). The solution of (2.14) is computed numerically using the finite-element software COMSOL Multiphysics 6.0. We refer to Appendix A for further details about the numerical solution.

3.1. *Constant advection closure*

In the constant advection closure problem, we specify the advective velocity in (2.14) as a constant field (2.18), obtaining (2.20). The solutions for the couples (M_{nn}, M_{tn}), (M_{nt}, M_{tt}) are presented in figure 3. To compact the notation, we introduce $\breve{u}_i = \epsilon Re_L(\mathcal{U}/\mathcal{U}^{\mathbb{O}})\bar{u}_i^{\mathbb{O}}$ in the term in front of the convective term on the left-hand side of (2.20), the inertia-driven coupling term with the macroscopic problem. We consider three values of $\breve{u}_i$, corresponding to the pure diffusive case ($\breve{u}_i = 0$; panels *b*, *e*), a case of pure normal advection ($\breve{u}_n \neq 0$ and $\breve{u}_t = 0$; panels *c*, *f*), and a case of normal and tangential advection ($\breve{u}_n \neq 0, \breve{u}_t \neq 0$; panels *d*, *g*). Recirculating zones propagate downstream the inclusion in

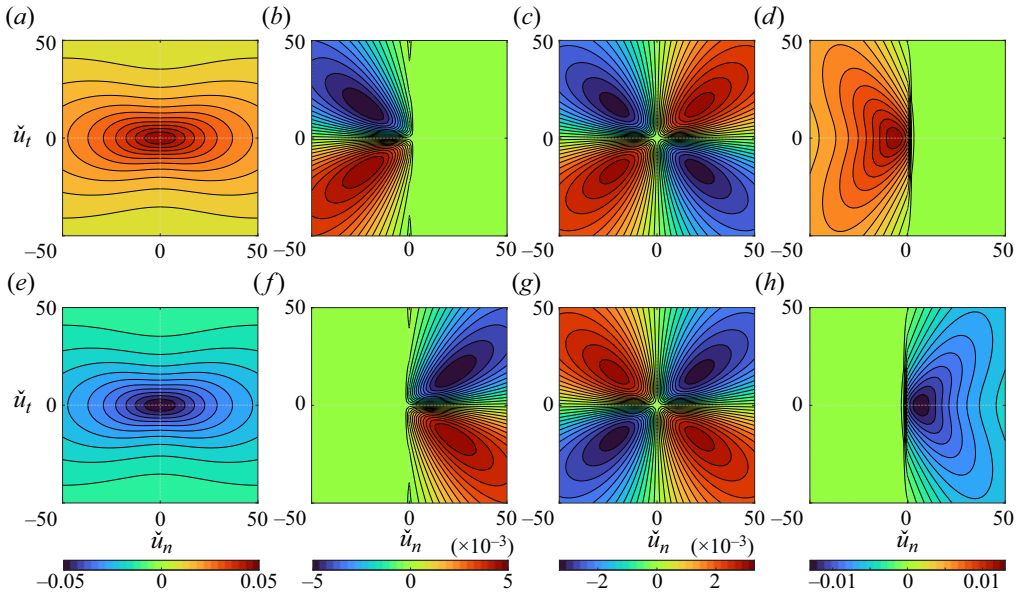

Figure 4. Average hydrodynamic tensor components, obtained by applying (2.15) to a range of constant advection closure solutions like those presented in figure 3. (*a*) $\bar{M}_{nn}$, (*b*) $\bar{M}_{nt}$, (*c*) $\bar{M}_{tn}$, (*d*) $\bar{M}_{tt}$, (*e*) $\bar{N}_{nn}$, (*f*) $\bar{N}_{nt}$, (*g*) $\bar{N}_{tn}$, (*h*) $\bar{N}_{tt}$.

the direction of the advective flow. Note that the same microscopic behaviour is noticed for N_{ij}, which satisfies $N_{ij}(\breve{u}_i) = -M_{ij}(-\breve{u}_i)$, and it is hence not shown.

By applying the averaging operators (2.15) and (2.16) to these fields for $\breve{u}_i$ in the range $[-50, 50]$, we obtain the maps of $\bar{M}_{ij}, \bar{N}_{ij}$. Figure 4 shows the contours of $\bar{M}_{ij}$ and $\bar{N}_{ij}$ as functions of $\breve{u}_i$. The off-diagonal components of $\bar{M}_{ij}, \bar{N}_{ij}$ are zero when $\breve{u}_i = 0$. The $\cdot_{nt}$ and $\cdot_{tt}$ components show a strong asymmetry with respect to $\breve{u}_n$. The permeability $\bar{M}_{nn}$ (figure 4*a*) is instead symmetric with respect to both components of $\breve{u}_i$ and shows a maximum for $\breve{u}_i = 0$. This suggests that inertia always decreases the permeability unless both the off-diagonal components are non-zero and partially compensate for the diminished $\bar{M}_{nn}$. Similar considerations apply to $\bar{N}_{ij}$, since $\bar{M}_{ij}(\breve{u}_k) = -\bar{N}(-\breve{u}_k)$. To confirm this observation, we propose a comparison of $\bar{M}_{nn}$ values with theoretical and experimental results from Jensen, Valente & Stone (2014*b*) in Appendix D.

We consider now the problem for T and S. We parametrize T and S in terms of the quantities appearing in the advective term, compacted as $\tilde{u}_i = \epsilon Pe_L(\mathcal{U}/\mathcal{U}^{\mathbb{O}})\bar{u}_i^{\mathbb{O}}$. Figure 5 shows T and S in the pure diffusive case (panels *a*,*d*), an advective case with $\tilde{u}_n = 100$, $\tilde{u}_t = 0$ (panels *b*,*e*) and a case with $\tilde{u}_n = \tilde{u}_t = 100$ (panels *c*,*f*).

Maps of $\bar{T}$ are obtained by averaging T using (2.15) and (2.16) for $\tilde{u}_i \in [-100, 100]$ (figure 6). We notice that $\bar{T}(\tilde{u}_i, \tilde{u}_t) = \bar{T}(\tilde{u}_n, -\tilde{u}_t)$ and that the maximum (minimum) of $\bar{T}$ ($\bar{S}$) is attained for a non-zero $\tilde{u}_n$. This suggests that advection increases the effective diffusivity $\bar{T}$. Similar considerations apply for S fields, which obey $\bar{S}(\tilde{u}_i) = -\bar{T}(-\tilde{u}_i)$. Eventually, the advective velocity can cause recirculating zones or concentration wakes downstream of the inclusions, with non-zero off-diagonal components of the tensors even in the absence of geometrical asymmetry (cf. figure 4*b*,*c*,*f*,*g*).

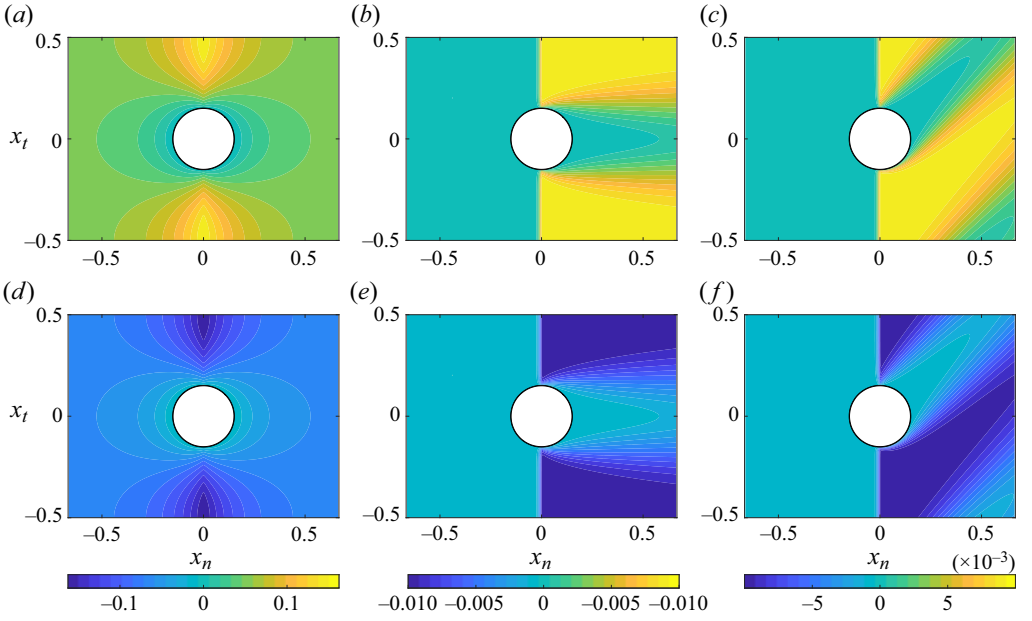

Figure 5. Solute concentration fields within the microscopic domain with different advective velocities $\tilde{u}_i$ obtained by solving the second two problems in the constant advection closure (2.20) around a circular solid inclusion. Contours of (*a–c*) T and (*d–f*) S for (*a*,*d*) $\tilde{u}_n = \tilde{u}_t = 0$, (*b*, *e*) $\tilde{u}_n = 100$, $\tilde{u}_t = 0$ and (*c*,*f*) $\tilde{u}_n = \tilde{u}_t = 100$ obtained using the constant advection closure approach.

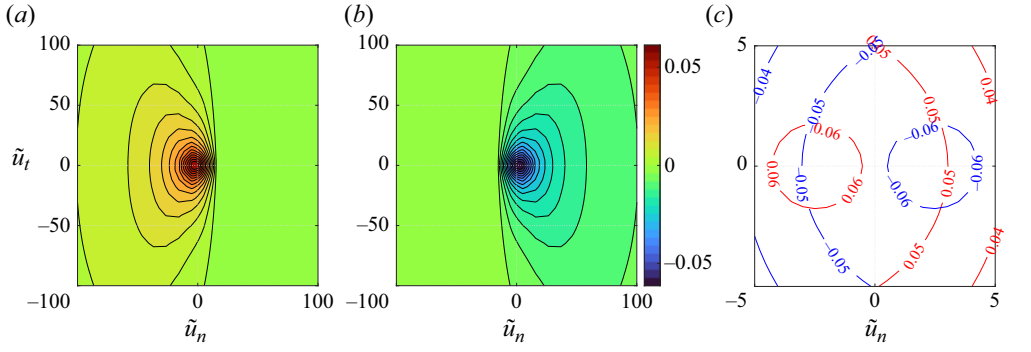

Figure 6. Average effective diffusivities, obtained by applying (2.16) to a range of constant advection closure solutions like those presented in figure 5. Contours of (*a*) $\bar{T}$ and (*b*) $\bar{S}$ as a function of the advection velocity components $\tilde{u}_n$, $\tilde{u}_t$ obtained using the constant advection closure approach. (*c*) A zoom-in on the region where the maximum and minimum of $\bar{T}$ (blue) and $\bar{S}$ (red) are attained.

3.2. *Variable advection closure*

In the variable advection closure problem, we specify the advective velocity in (2.14) as a variable field, see (2.19), obtaining (2.21). The solutions for M_{ij} and N_{ij} are presented in figure 3. The advective term depends on four parameters, $\check{\Sigma}_{ij}^{\mathbb{U},\mathbb{D}} = \epsilon^2 Re_L^2 (\mathcal{U}/\mathcal{U}^{\mathbb{O}}) \Sigma_{ij}^{\mathbb{U},\mathbb{D}} n_j$ for the hydrodynamic problem and four parameters $\tilde{\Sigma}_{ij}^{\mathbb{U},\mathbb{D}} = \epsilon^2 Pe_L (\mathcal{U}/\mathcal{U}^{\mathbb{O}}) \Sigma_{ij}^{\mathbb{U},\mathbb{D}} n_j$ for the advection–diffusion problem (T, S). In figure 7, the effect of $\check{\Sigma}_{ij}^{\mathbb{U},\mathbb{D}}$ is shown for variations of some sample components of M_{ij}. The application of a non-zero stress component along

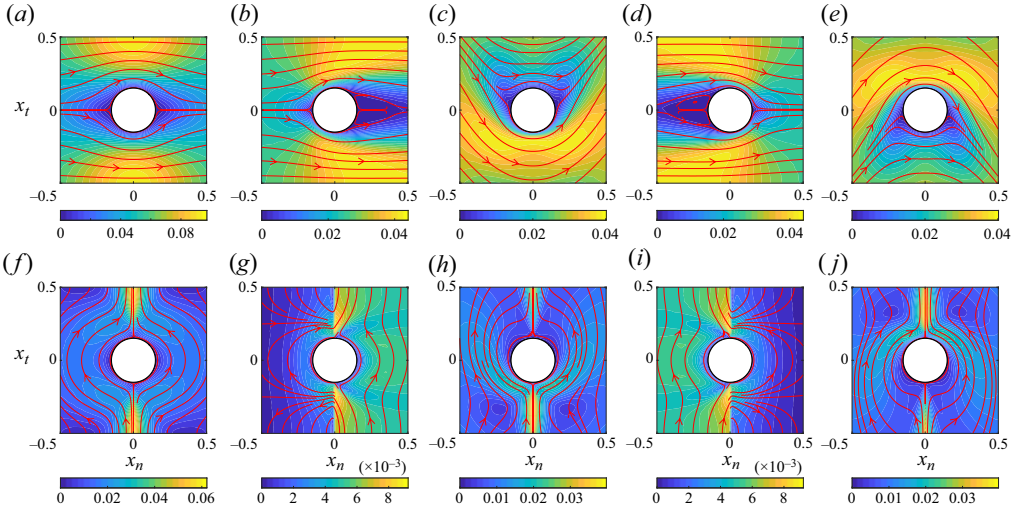

Figure 7. Flow fields within the microscopic domain with different advective velocities $\check{\Sigma}_{ij}$ obtained by solving the first two problems in the constant advection closure (2.21) around a circular solid inclusion. Magnitude iso-contours and streamlines (red) of (*a–e*) (M_{nn}, M_{tn}) and (*f–j*) (M_{nt}, M_{tt}) for five different combinations of $\check{\Sigma}_{ij}^{\mathbb{U},\mathbb{D}}$. (*a*,*f*) $\check{\Sigma}_{ij}^{\mathbb{U},\mathbb{D}} = \epsilon^2 Re_L^2 \Sigma_{ij}^{\mathbb{U},\mathbb{D}} = 0$; (*b*,*g*) $\check{\Sigma}_{nn}^{\mathbb{U}} = 2500$, (*c*,*h*) $\check{\Sigma}_{tn}^{\mathbb{U}} = 2500$, (*d*,*i*) $\check{\Sigma}_{nn}^{\mathbb{D}} = 2500$ and (*e*,*j*) $\check{\Sigma}_{tn}^{\mathbb{D}} = 2500$. For each case, the components of $\check{\Sigma}_{ij}^{\mathbb{U},\mathbb{D}}$ not specified are equal to zero. The variable advection closure is employed.

a given direction causes the flow to deviate along that direction, eventually developing a laminar separation bubble downstream (for $\check{\Sigma}_{nn}$ with the same sign of the Dirac forcing) or upstream the inclusion (for $\check{\Sigma}_{nn}$ with opposed sign with respect to the Dirac forcing). By applying the averaging operators (2.15) and (2.16) to M_{ij} and N_{ij}, the iso-levels of $\bar{M}_{ij}, \bar{N}_{ij}$ are obtained for varying $\check{\Sigma}_{ij}^{\mathbb{U},\mathbb{D}}$ (cf. figure 8). This figure represents a sampling on a two-dimensional (2-D) sub-manifold of the four-dimensional (4-D) manifold where the averaged tensors live. Further sub-manifolds are presented in Appendix B for other values of $\check{\Sigma}_{ij}^{\mathbb{U},\mathbb{D}}$. The $\bar{M}_{nn}$ and $\bar{N}_{nn}$ terms show symmetry about two axes also in this case, while $\bar{M}_{ij}(\check{\Sigma}_{ij}^{\mathbb{U},\mathbb{D}}) = -N(-\check{\Sigma}_{ij}^{\mathbb{U},\mathbb{D}})$. The maxima of permeability ($\bar{M}_{nn}$) are found in the case of Stokes flow (i.e. balanced $\check{\Sigma}_{ij}^{\mathbb{U}}$ and $\check{\Sigma}_{ij}^{\mathbb{D}}$ contributions). Slip ($\bar{M}_{tt}$) has a maximum for values of $\check{\Sigma}_{nn}^{\mathbb{U}}$ close to $\check{\Sigma}_{nn}^{\mathbb{D}}$, but not exactly corresponding to Stokes' flow.

The variable advection approach applied to the problem for T and S in (2.14) gives (2.21). Its solution requires the tensors M_{ij} and N_{ij} to be known. For simplicity, we consider the case of diffusive momentum transport ($Re_L = 0$, panel *a*, corresponding to $\bar{M}_{nn} = 0.05$, $\bar{M}_{nn} = 0.01$, $\bar{M}_{nt} = \bar{M}_{tn} = 0$ and $\bar{N}_{ij} = -\bar{M}_{ij}$). The microscopic field T is presented in figure 9 for different values of $\tilde{\Sigma}_{ij}^{\mathbb{U},\mathbb{D}}$. Here, T exhibits a wake directed as the dominant inertial component for each case. By applying the average operator (2.15) and (2.16), we obtain the contours of $\bar{T}$ for $\tilde{\Sigma}_{ij}^{\mathbb{U},\mathbb{D}} \in [-50, 50]$. Interestingly, in the considered range, there is a negligible influence of $\tilde{\Sigma}_{tn}^{\mathbb{U},\mathbb{D}}$, while $\tilde{\Sigma}_{nn}^{\mathbb{U},\mathbb{D}}$ is dominant in this problem. Similar considerations apply to $\bar{S}$, since $\bar{T}(\tilde{\Sigma}_{nn}^{\mathbb{U},\mathbb{D}}) = -\bar{S}(-\tilde{\Sigma}_{nn}^{\mathbb{U},\mathbb{D}})$.

In this section, we presented relevant features of the microscopic flow occurring for non-negligible inertia. The microscopic solutions depend on the pore geometry and flow characteristics. A comparison of figures 6 and 10 shows that T depends strongly on $\tilde{u}_t$ but

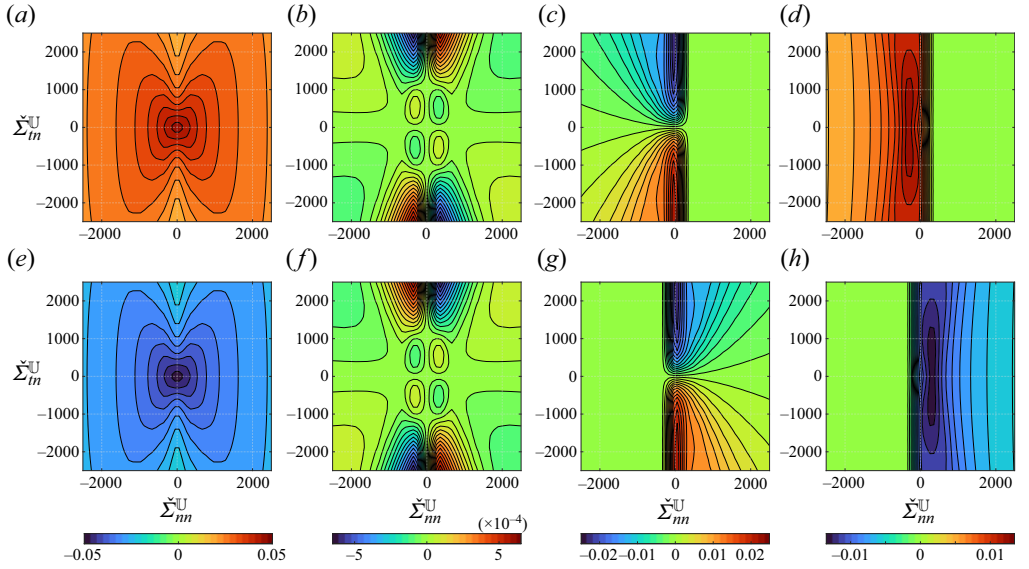

Figure 8. Average hydrodynamic tensor components, obtained by applying (2.15) to a range of variable advection closure solutions like those presented in figure 7. Iso-contours of average tensor component (*a*) $\bar{M}_{nn}$, (*b*) $\bar{M}_{nt}$, (*c*) $\bar{M}_{tn}$, (*d*) $\bar{M}_{tt}$, (*e*) $\bar{N}_{nn}$, (*f*) $\bar{N}_{nt}$, (*g*) $\bar{N}_{tn}$, (*h*) $\bar{N}_{tt}$ for $(\check{\Sigma}^{\mathbb{U}}_{nn}, \check{\Sigma}^{\mathbb{U}}_{tn}) \in [-2500, 2500]$, while $\check{\Sigma}^{\mathbb{D}}_{\cdot n} = 0$. The variable advection closure approach is exploited.

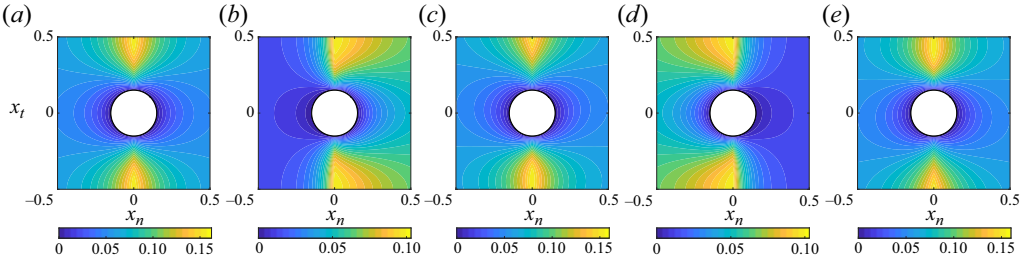

Figure 9. Solute concentration fields within the microscopic domain with different advective velocities $\tilde{\Sigma}_{ij}$ obtained by solving the second two problems in the variable advection closure (2.21) around a circular solid inclusion. Iso-contours of the effective diffusivity T computed using the variable advection closure model. (*a*) $\tilde{\Sigma}^{\mathbb{U},\mathbb{D}}_{ij} = 0$, (*b*) $\tilde{\Sigma}^{\mathbb{U}}_{nn} = 100$, (*c*) $\tilde{\Sigma}^{\mathbb{U}}_{tn} = 100$, (*d*) $\tilde{\Sigma}^{\mathbb{D}}_{nn} = 100$ and (*e*) $\tilde{\Sigma}^{\mathbb{D}}_{tn} = 100$. For each panel, the components of $\tilde{\Sigma}^{\mathbb{U},\mathbb{D}}_{ij}$ not mentioned are equal to zero.

not on $\tilde{\Sigma}^{\mathbb{U},\mathbb{D}}_{tn}$. However, this apparent discrepancy can be explained by considering that not all points in figure 6 are images of points in figure 10 through (2.17). The range represented in figure 10 thus corresponds only to a thin zone around the axis $\tilde{u}_t = 0$ in figure 6.

4. Comparison between full-scale simulations and homogenized model

In this section, we compare the macroscopic solution against simulations of the flow solved at all scales. We consider a two-dimensional flat membrane composed of circular inclusions with spacing $\ell/L = \epsilon = 0.1$, invested by a uniform stream. The computational domain is depicted in figure 11. Dirichlet boundary conditions on the velocity $(u_x, u_y) = (\sin\alpha, \cos\alpha)$ are imposed on the bottom and left sides of the domain, while

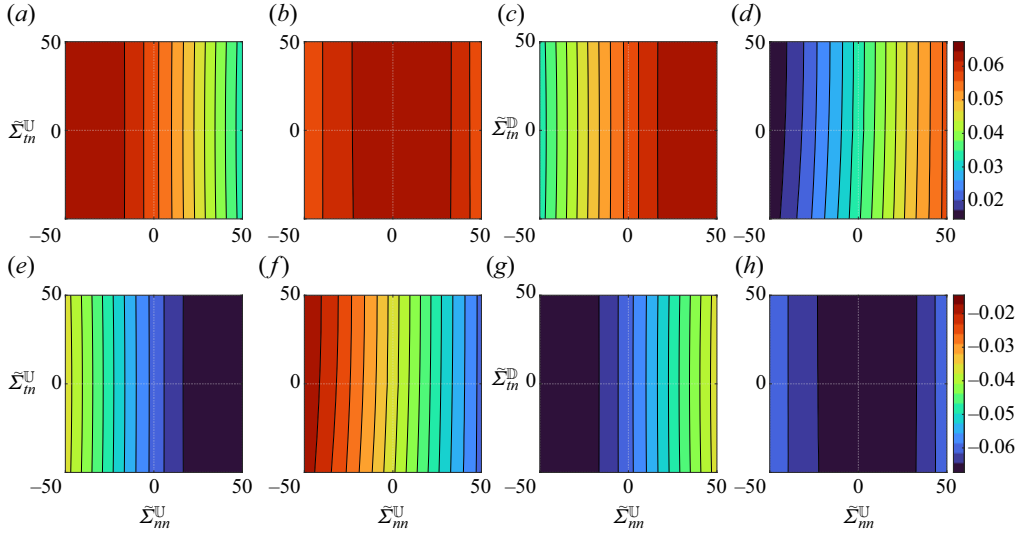

Figure 10. Average effective diffusivities, obtained by applying (2.16) to a range of variable advection closure solutions like those presented in figure 9. Contours of (*a–d*) $\tilde{T}$ and (*e–h*) $\tilde{S}$. Each panel is obtained for a different value of $\tilde{\Sigma}^{\mathbb{U},\mathbb{D}}_{ij}$; (*a*,*e*) $\tilde{\Sigma}^{\mathbb{D}}_{nn} = \tilde{\Sigma}^{\mathbb{D}}_{tn} = 0$, (*b*,*f*) $\tilde{\Sigma}^{\mathbb{D}}_{nn} = \tilde{\Sigma}^{\mathbb{D}}_{tn} = 50$, (*c*,*g*) $\tilde{\Sigma}^{\mathbb{U}}_{nn} = \tilde{\Sigma}^{\mathbb{U}}_{tn} = 0$, (*d*,*h*) $\tilde{\Sigma}^{\mathbb{U}}_{nn} = \tilde{\Sigma}^{\mathbb{U}}_{tn} = 50$. The stress tensor components not mentioned in each panel are equal to zero. The variable advection closure approach is considered.

a Neumann condition $\Sigma_{ij} n_j = 0$ is imposed at the top and right sides of the domain. The no-slip condition $u_i = 0$ is imposed on the surface of the inclusions $\partial\mathbb{M}$. For the solute concentration c, the Dirichlet condition $c = 1$ applies on the left side of the domain, while $c = 0$ is imposed on $\partial\mathbb{M}$. Zero-flux conditions apply on the external sides of the domain. The domain decomposition method (Quarteroni 2017) is employed to solve the macroscopic configuration by splitting the domain into two regions (cf. figure 11*b*) connected by the membrane's homogenized condition (2.17) on $\mathbb{C}$. Continuity of velocity and stresses are imposed on the fluid–fluid interfaces, identified by the dashed lines in figure 11(*b*). The macroscopic simulations are solved iteratively using a fixed-point scheme:

(i) the macroscopic problem is solved using the Stokes solution;

(ii) the values of $\check{u}_i, \tilde{u}_i$ (for the constant advection closure approach) or $\check{\Sigma}^{\mathbb{U},\mathbb{D}}_{ij}, \tilde{\Sigma}^{\mathbb{U},\mathbb{D}}_{ij}$ (for the variable advection closure approach) are sampled along the surface $\mathbb{C}$ cell-by-cell (i.e. by computing their average value in each segment of length ℓ on $\mathbb{C}$). This additional averaging of the velocity profile aligns with the need to match the continuous macroscopic solution with a discrete number of microscopic cells that form the membrane and is asymptotically coherent as long as variations of the local velocity from the average are of order $O(\epsilon^2)$. In the ideal theoretical limit as $\epsilon \to 0$, the point-wise macroscopic velocity would replace the cell-by-cell average; however, this scenario is never encountered in real membrane geometries. We assumed $\mathcal{U}/\mathcal{U}^{\mathbb{O}} \sim 1$ in the present computations. However, when $\mathcal{U}/\mathcal{U}^{\mathbb{O}} \ll 1$ (like the case of flow purely tangential to the membrane), taking $\mathcal{U}/\mathcal{U}^{\mathbb{O}}$ as the average macroscopic velocity on the membrane is a cheaper alternative;

(iii) we substitute these values into the microscopic problems in (2.14);

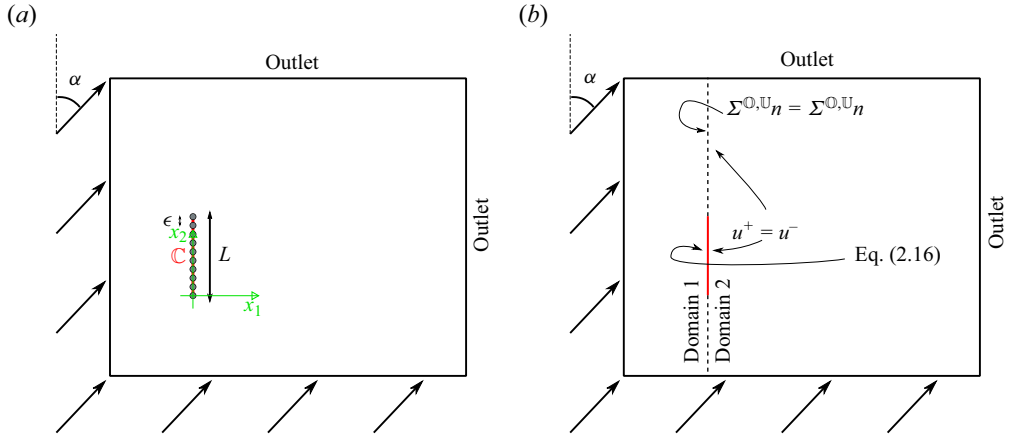

Figure 11. (*a*) Full-scale computational domain. Arrows correspond to a Dirichlet boundary condition on velocity (inlet), and outlet boundary condition corresponds to imposing $\Sigma_{ij}n_j = 0$. No slip is applied on the membrane walls. The origin of the axes is placed at the lowest end of the membrane, and the domain extends for $x_1 \in [-1.5L, 5.5L]$ and $x_2 \in [-1.5L, 3.5L]$. (*b*) Purely macroscopic computational domain. The full domain is separated into an upward and a downward domain by membrane centreline $\mathbb{C}$ (red).

(iv) we solve again the macroscopic simulation with the new distribution of microscopic tensors, constant on each cell of length ℓ and changing discontinuously between cells to get an updated version of the closure advection to be fed within the microscopic problems;
(v) we iterate the procedure until convergence.

The convergence criterion is satisfied when the difference between two subsequent computations in terms of (u_i, c) on $\mathbb{C}$ is below 1 % of their mean values cell-by-cell. At each iteration, we perform $1/\epsilon$ microscopic (since the membrane is made of $1/\epsilon$ cells of length ℓ, for a total length of L) and one macroscopic computation, with an averaging step in between. The comparison between the macroscopic model and the full-scale solution is performed in terms of averaged values of velocity and concentration on the membrane and point-wise values of the velocity, pressure and concentration fields far from the membrane. For simplicity, we compare separately the solvent and solute transport, which corresponds to considering $Re_L \neq 0$, $Pe_L = 0$ (§ 4.1) and $Re_L = 0$, $Pe_L \neq 0$ (§ 4.2), respectively.

4.1. *Mass and momentum conservation*

In this section, we focus on the solvent flow with $Re_L = 400$, $\epsilon = 0.1$ and $\alpha = 75^\circ$. In figure 12, we observe a wake developing downstream of each inclusion, forming a macroscopic wake downstream of the membrane, with parabolic-like velocity profiles across the openings of the membrane. Figure 13 shows the relative differences in the fields between the full-scale and homogenized models. The largest discrepancies are found in the region immediately downstream of the membrane. These discrepancies decrease from the Stokes to the constant and variable advection closure models (panels *a*, *c* and *b*, respectively), confirming that the quasi-linear models well capture the flow structures for non-negligible inertial effects and the variable advection model is a faithful approximation of the Navier–Stokes solution at the microscopic scale. Figure 14 shows the values of $\bar{M}_{ij}$ and $\bar{N}_{ij}$ sampled on the membrane. The difference between the values of $\bar{M}_{ij}$ found using the Stokes and the constant and variable advection models is evident, in particular

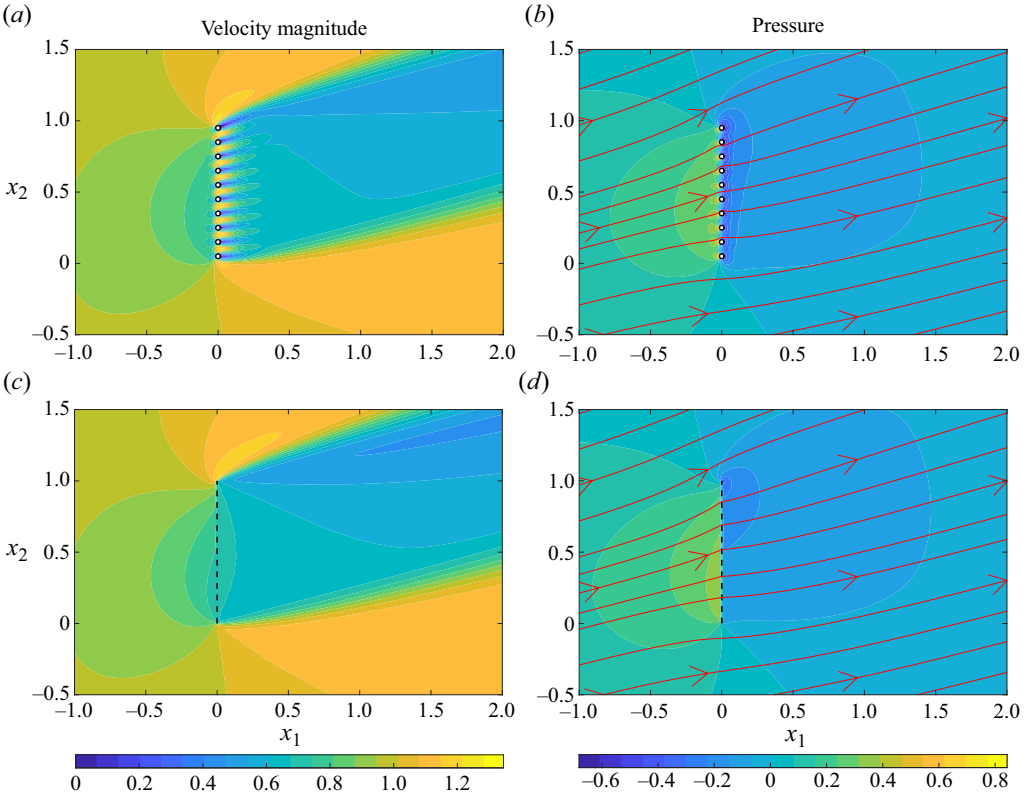

Figure 12. (*a*,*c*) Velocity magnitude and (*b*,*d*) pressure iso-contours with velocity streamlines superimposed in the proximity of the membrane for (*a*,*b*) a full-scale and (*c*,*d*) a variable-advection macroscopic simulation for $\alpha = 75^\circ$, $\epsilon = 0.1$ and $Re_L = 400$. Black dashes indicate the location of the fictitious interface.

for the off-diagonal components. When advection is considered, the components $\cdot_{nn}$ and $\cdot_{tt}$ show a nearly constant value along the membrane which is different from the value predicted by the Stokes model. A comparison of the velocity fields at the membrane centreline $\mathbb{C}$ is presented in figure 15 and confirms the accuracy observed in figure 13. We consider also two sampling lines at $x_1 = \pm\epsilon/2$, i.e. on the two sides of the interface, presented in figure 15(*c*). Pressure, sampled at $x_1 = \pm\epsilon/2$, is captured more accurately by the constant advection and the variable advection models than by the Stokes model. Figure 16 shows local comparisons on the $x_2 = 0.5$ lines, exhibiting a good agreement between the full-scale and macroscopic fields far from the membrane.

To assess the robustness of the previous observations, we vary Re_L, ϵ and α, and quantitatively evaluate the agreement between the full-scale solution and the macroscopic models via a global error defined as

$$e_g = \sqrt{\bar{e}_r(||\boldsymbol{u}||)^2 + \bar{e}_r(|p|)^2}, \tag{4.1}$$

where $\bar{e}_r$ is the mean of the point-wise relative error between the considered macroscopic model and the full-scale solution in the computational domain. Figure 17(*a*) shows the errors calculated for several configurations such that $\epsilon = 0.1$, $\alpha \in [0^\circ, 90^\circ]$ and $Re_L \in [200, 1000]$. Going from Stokes to constant and variable advection models, an overall decrease of e_g is noticed. Figure 17(*b*) presents the dependence of e_g on the velocity at the

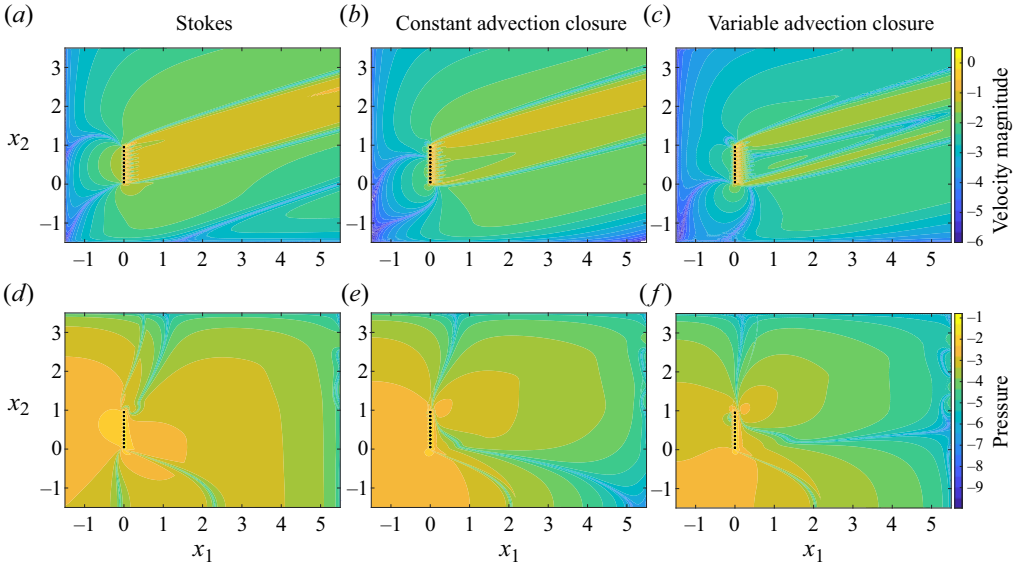

Figure 13. Contours of the relative error of (*a–c*) velocity magnitude and (*d–f*) pressure between the full-scale solution and the macroscopic models. Panels (*a*,*d*) refer to Stokes models, while panels (*b*,*e*) and (*c*,*f*) to the constant and variable advection closure, respectively. Fluid-flow and geometry parameters are $\alpha = 75^\circ$, $\epsilon = 0.1$ and $Re_L = 400$. Colourbar is in $\log_{10} e_r(\cdot)$-scale.

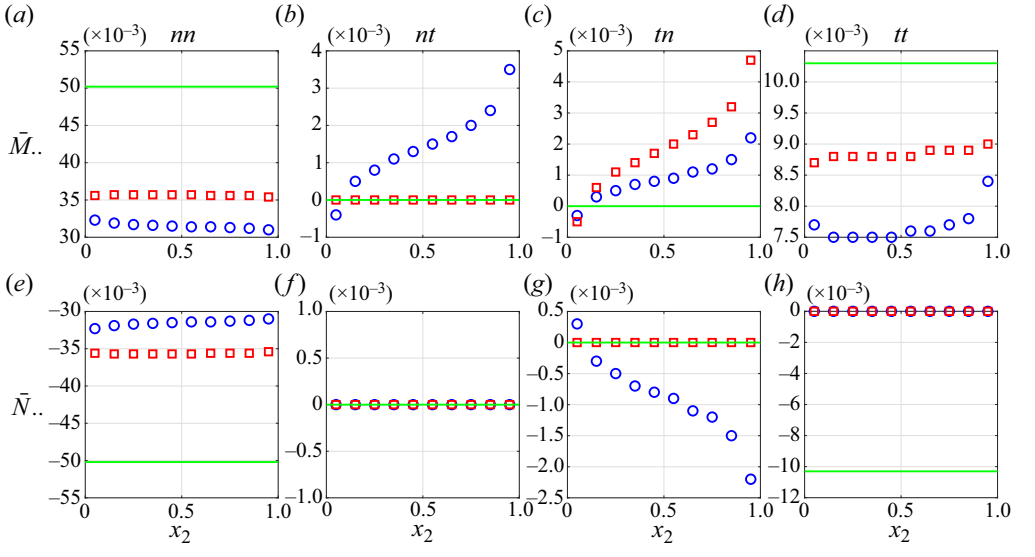

Figure 14. Averaged tensor values (*a*) $\bar{M}_{nn}$, (*b*) $\bar{M}_{nt}$, (*c*) $\bar{M}_{tn}$, (*d*) $\bar{M}_{tt}$, (*e*) $\bar{N}_{nn}$, (*f*) $\bar{N}_{nt}$, (*g*) $\bar{N}_{tn}$ and (*h*) $\bar{N}_{tt}$ for $Re_L = 400$, $\alpha = 75^\circ$, $\epsilon = 0.1$ with the Stokes (green line), constant advection closure (blue circles) and variable advection closure (red squares) problems.

membrane as a function of ϵ for $Re_\ell \approx \epsilon Re_L = 75$. Here, $\alpha = 90^\circ$ for all computations. The error computed for the Stokes and the variable advection model shows nearly an order of magnitude of difference, with opposite trends as a function of ϵ (keeping ϵRe_L constant).

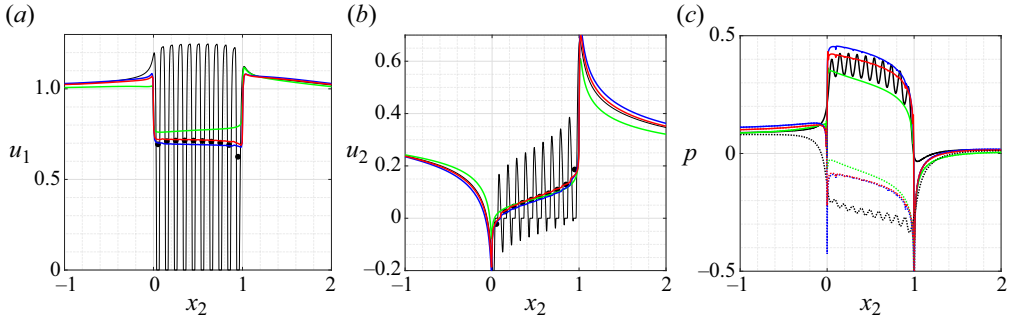

Figure 15. (*a*) Horizontal and (*b*) vertical velocity and (*c*) pressure. In panels (*a*,*b*), velocity values are sampled on the membrane centreline ($x_1 = 0, x_2 \in [-1, 2]$) in the full-scale solution and on the fictitious interface in the macroscopic simulations. In panel (*c*), the pressure values are sampled at $x_1 = \pm\epsilon/2$ and presented as dotted and full lines, respectively. Colour code, full-scale solution (black lines); averaged full-scale solution (black dots); constant (blue) and variable (red) advection closure; Stokes case (green). Configuration parameters are $\alpha = 75^\circ$, $\epsilon = 0.1$ and $Re_L = 400$.

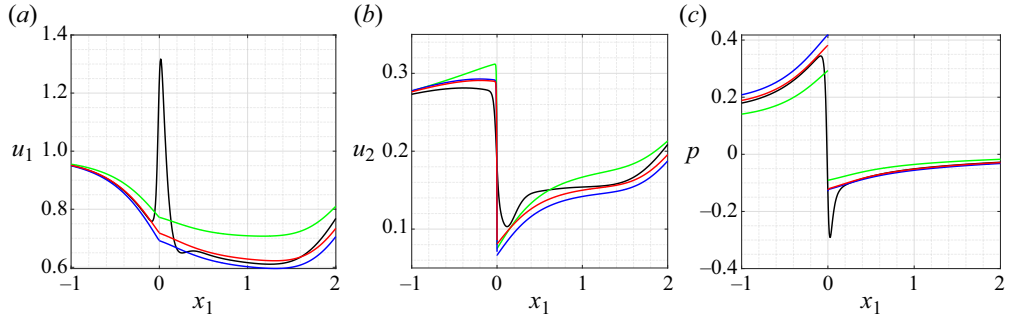

Figure 16. (*a*) Horizontal and (*b*) vertical velocity and (*c*) pressure sampled along a line at $x_2 = 0.5$ and $x_1 \in [-1, 2]$. The same colour code and configuration parameters as in figure 15 are used.

An additional test case, the flow in a channel vertically split by a membrane, is considered in Appendix C.

4.2. *Solute flux conservation*

We consider the case of $Pe_L > 0$. To increase Pe_L, we decrease the diffusivity D while Re_L remains negligible. This allows us to assess the reliability of the model independently of the solvent flow approximation. We consider a set-up with $\alpha = 90^\circ$, $\epsilon = 0.1$ and $Pe_L = 1000$. The iso-contours of the flow fields solved at all scales are presented in figure 18. The velocity field (panel *a*) shows a small wake downstream of the membrane. The macroscopic flow does not present a re-circulation region, coherent with the hypothesis of negligible inertia. Conversely, the effect of the finite Péclet number is evident in panel (*b*), where the solute concentration iso-levels are aligned with the solvent flow streamlines. The $\bar{T}$ and $\bar{S}$ values found in the present flow configuration using the different models are collected in figure 19. The values of $\bar{T}$ and $\bar{S}$ found using the Stokes and constant advection model are quite similar, as opposed to those obtained using the variable advection model.

The variable advection model shows larger differences with respect to the Stokes solution compared with those with the constant advection closure model. We present a

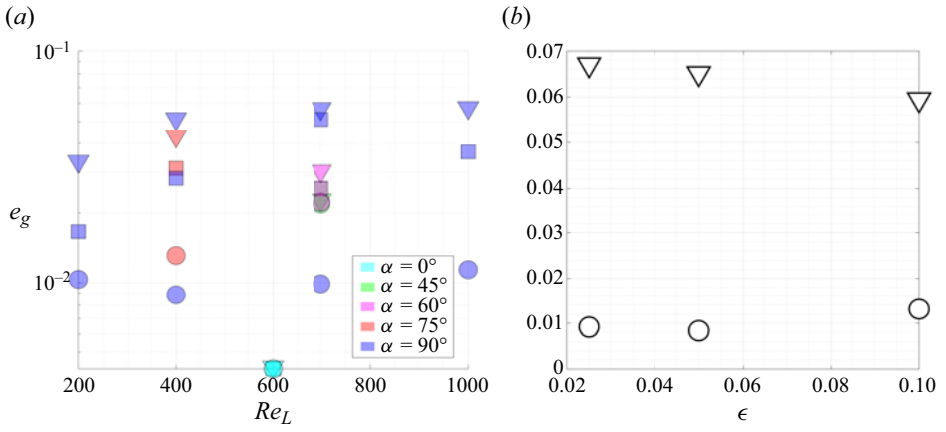

Figure 17. (*a*) Global error e_g defined in (4.1) for macroscopic simulations having $\epsilon = 0.1$, and α ranging from $\alpha = 0°$ to 90° and Re_L from 200 to 1000. The values of α are represented using the colour code (legend in panel *a*), while the marker indicates the type of macroscopic model used to compute that data point (triangles for Stokes, squares for constant advection closure and circles for variable advection closure). (*b*) e_g for the Stokes and variable advection closure model for different values of ϵ. All simulations have $Re_\ell = 75$ and $\alpha = 90°$. A constant value of $Re_\ell = 75$ has been realized by choosing the (ϵ, Re_L) couples as (0.1, 750), (0.05, 1500) and (0.025, 3000). Same marker code as for panel (*a*).

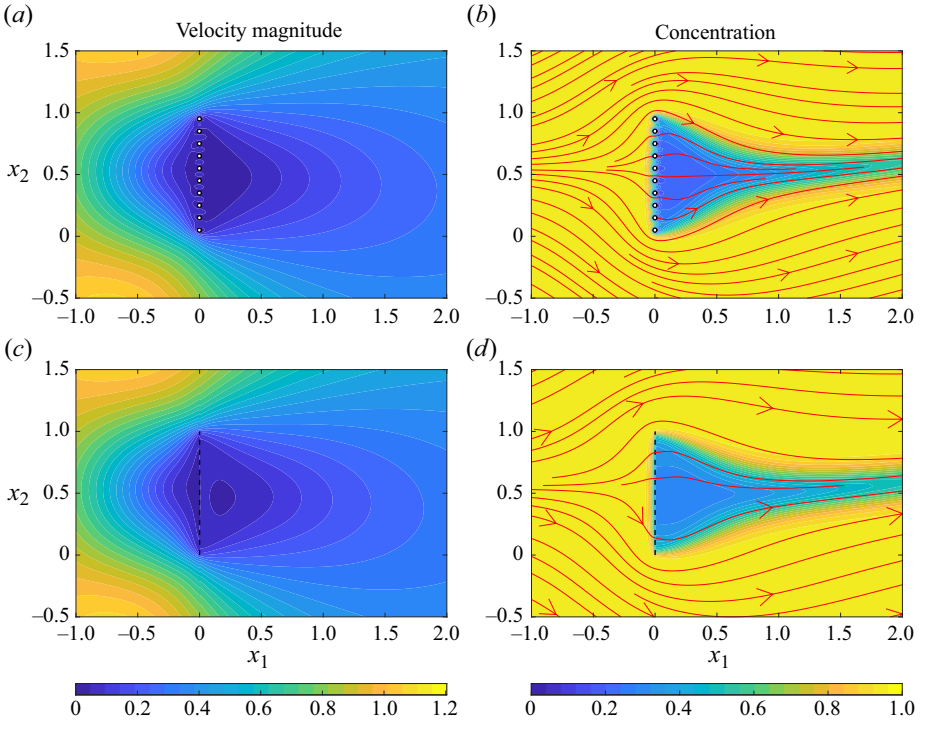

Figure 18. (*a*,*c*) Velocity magnitude and (*b*,*d*, red lines) concentration iso-contours with velocity streamlines for (*a*,*b*) a full-scale and (*c*,*d*) a variable-advection macroscopic solution at $Re_L = 0$, $Pe_L = 1000$, $\alpha = 90°$ and $\epsilon = 0.1$. Black dashes indicate the location of the fictitious interface.

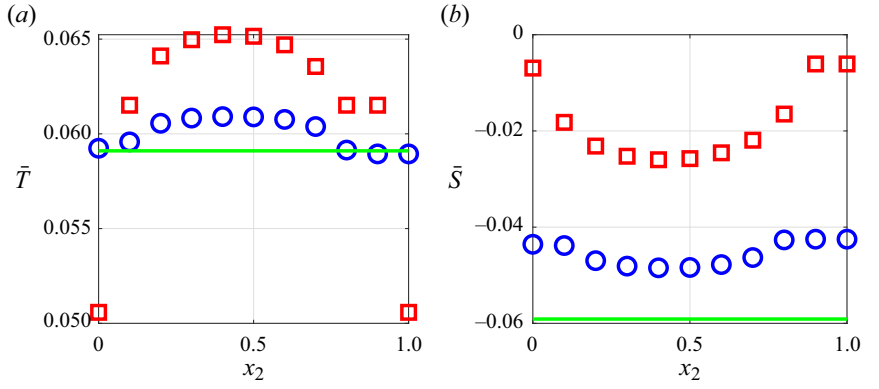

Figure 19. Values of (*a*) $\bar{T}$ and (*b*) $\bar{S}$ along the membrane for Stokes (green line), constant advection closure (blue circles) and variable advection closure (red squares). The flow parameters are $\alpha = 90^\circ$, $\epsilon = 0.1$, $Pe_L = 1000$ and $Re_L = 0$.

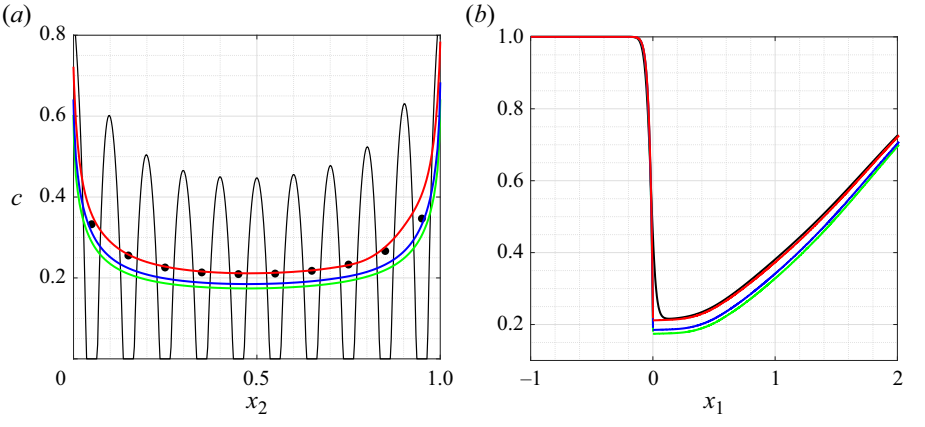

Figure 20. Comparison between the values of concentration c sampled (*a*) on the membrane centreline $\mathbb{C}$ or (*b*) on the membrane axis, corresponding to a line at $x_2 = 0.5$ and $x_1 \in [-1, 2]$. The same colour coding as in figure 15 has been adopted. The flow parameters are $\alpha = 90^\circ$, $\epsilon = 0.1$, $Pe_L = 1000$ and $Re_L = 0$.

comparison of the concentration values on the membrane ($x_1 = 0$) and its axis ($x_2 = 0.5$) in figure 20. The variable advection closure approach shows a good agreement with the full-scale solution both on the membrane (panel *a*) and in the far-field, represented by the values of solute concentration sampled on the membrane axis (panel *b*). The constant advection closure offers little improvement in terms of accuracy, compared with the Stokes case. We conclude that the maximum accuracy for the case of finite Péclet number is found using the variable advection closure, in analogy with the non-zero Reynolds number case. The quasi-linear homogeneous model is thus more accurate than the Stokes model. In addition, the variable advection approach shows a better agreement with full-scale simulations than the constant advection approach. However, we observe that the new macroscopic approximations are computationally more expensive than the Stokes model. Models of engineering interest used in preliminary design phases need to provide a fast and accurate output which can be used as a starting point for more expensive computations. In the following section, we discuss the trade-off between accuracy and computational efficiency, a key aspect of industrial flow modelling.

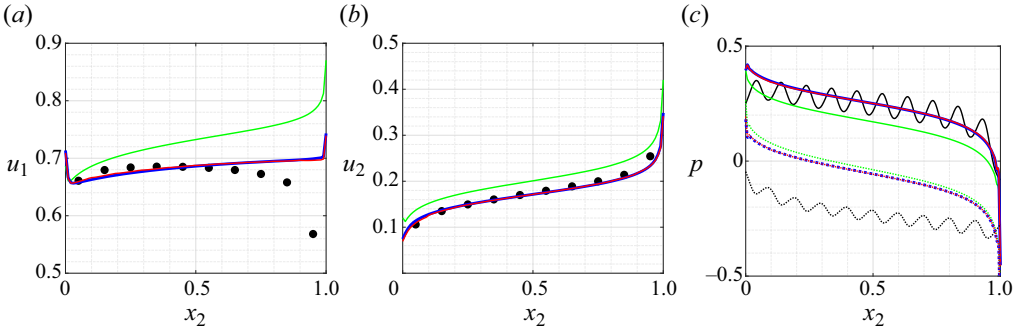

Figure 21. Comparison between the (*a*) averaged full-scale solution normal velocity, (*b*) tangential velocity and (*c*) pressure. Velocity components are sampled on the membrane centreline $\mathbb{C}$ in the full-scale solution and the fictitious interface in the macroscopic cases ($x_1 = 0, y \in [0, 1]$). Pressure is sampled on two lines parallel to $\mathbb{C}$ and distant $\pm\epsilon/2$ (dotted and full lines, respectively). The colour code is common to all panels: black dots for the cell-averaged values of the full-scale solution, green lines for the Stokes model, red lines for the variable advection closure unclustered model and blue lines for the variable advection closure, clustered model. The flow and geometry parameters are $\alpha = 60^\circ$, $Re_L = 700$, $\epsilon = 0.1$.

5. Towards data-driven homogenization: improving the computational efficiency through a central-value approximation

The constant and variable advection closure models require the solution of (2.14) in each microscopic cell forming a single membrane, i.e. $1/\epsilon$ times at each iteration (or N/ϵ for N membranes whose inclusions have spacing ϵ). This leads to a loss in computational efficiency compared with the Stokes model, which requires only one microscopic solution without any iterative procedure. In the following, we propose a strategy to reduce the computational cost of the macroscopic solution focusing on the previously validated variable-advection approach. To avoid overloading this article, we consider only the hydrodynamic problem. However, the efficient solution strategy proposed in this section applies also to the constant advection model and advection–diffusion equations.

5.1. *Computing a single membrane using its central values*

The quantities $\mathcal{P} = (\check{u}_i, \tilde{u}_i, \check{\Sigma}_{ij}^{\mathbb{U},\mathbb{D}}, \tilde{\Sigma}_{ij}^{\mathbb{U},\mathbb{D}})$ affect the values of $\bar{M}_{ij}$, $\bar{N}_{ij}$, $\bar{T}$ and $\bar{S}$. We notice that the dispersion of $\bar{M}_{ij}$ and $\bar{N}_{ij}$ observed in figure 14 is small (less than 5 % of the mean membrane values for the three dominant components ($\bar{M}_{nn}$, $\bar{N}_{nn}$ and $\bar{M}_{tt}$) of the $\bar{M}_{ij}$ and $\bar{N}_{ij}$ tensors). For the simple geometry presented in figure 11, the central value of this dispersion roughly corresponds to the values of $\mathcal{P}$ evaluated at the membrane's centre. We can thus employ the values of $\mathcal{P}$ reached in the middle of the membrane in the evaluation of $\bar{M}_{ij}$, $\bar{N}_{ij}$, $\bar{T}$ and $\bar{S}$. To assess the validity of this approach, we consider the case $\alpha = 60^\circ$, $Re_L = 700$. Figure 21 presents a comparison of the cell-averaged values of the solvent velocity and pressure on the membrane obtained in the full-scale solution and using the Stokes and variable advection closure models, clustered (i.e. obtained using a single microscopic computation for all cells at each iteration) and unclustered (i.e. using one microscopic computation for each cell at each iteration). Figure 22 compares the solvent flow fields sampled along the axis of the membrane. In both figures 21 and 22, the variable advection closure clustered and unclustered versions predict very similar values of the flow fields. Average relative differences between the two approaches are of the order of 0.05ϵ, well below the accuracy of the homogeneous model ($O(\epsilon)$). In terms of computational

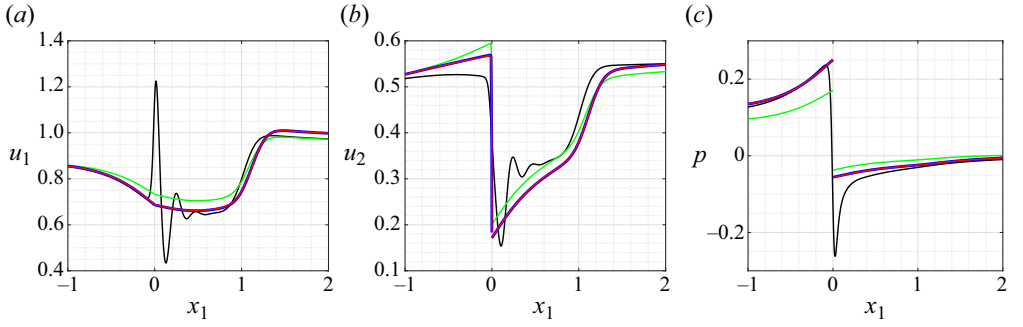

Figure 22. Comparison between flow field values of (*a*) normal velocity, (*b*) tangential velocity and (*c*) pressure sampled along the axis of the membrane, $x_2 = 0.5$, $x_1 \in [-1, 2]$. The same colour code as in figure 21 is adopted. The flow and geometry parameters are $\alpha = 60^\circ$, $Re_L = 700$, $\epsilon = 0.1$.

cost, the clustered version requires only one computation per iteration (similar to the Stokes solution), while the unclustered one requires $1/\epsilon$.

5.2. *Clustering the cells*

In the previous paragraph, the centre of the membrane was used to compute one set of approximate values of the tensors $\bar{M}_{ij}$ and $\bar{N}_{ij}$ in place of $1/\epsilon$ (i.e. one for each microscopic cell). Flow and geometry configurations of industrial interest are generally more complicated. We introduce a clustering algorithm in our macroscopic simulation workflow to automate the choice of a subset of flow conditions (i.e. of the $\mathcal{P}$ quantities) which can approximate the real, cell-wise distribution of $\mathcal{P}$. Given a set of length N of the flow quantities $\mathcal{P}$, we divide $\mathcal{P}$ into $K \leq N$ clusters in which each element belongs to the cluster with the nearest centroid. We thus represent the cluster using its centroid. Several algorithms for splitting datasets into clusters have been proposed in the literature, see Bishop (2006) for a review. Testing their relative performance in the present case goes beyond the scope of this work. For this reason, as an example, we choose the K-Means++ (Arthur & Vassilvitskii 2007), implemented in MATLAB 2023a. This algorithm splits a given set of data into a user-defined number of clusters according to a notion of distance, Euclidean in the present case. The optimal number of clusters can be found using some heuristic procedures, like the 'elbow rule' (Tibshirani, Walther & Hastie 2001), but the cluster distribution is sufficiently evident in this case that the iterative procedure can be avoided. Figure 23(*a*) shows the considered flow configuration. It consists of three identical membranes composed of circular inclusions with spacing $\epsilon = 0.1$, immersed in a free stream at $Re_L = 500$. Velocity magnitude iso-levels and velocity streamlines are presented in panel (*a*). On the top and bottom sides of the domain, a no-slip boundary condition is applied. The leftmost membrane is fully exposed to the flow, as well as the top portions of the other two membranes, while the bottom portions experience milder flow conditions. Panel (*b*) shows that the data are clustered in three or four blocks, corresponding to the different flow conditions at the cell level. By computing the microscopic cases using the $\Sigma_{ij}^{\mathbb{U},\mathbb{D}}$ of each cluster centroid, we solve the corresponding macroscopic computation. A comparison of the velocity at the membranes in the full-scale solution and the clustered variable advection closure macroscopic solution is presented in figure 24. The prediction based on the four clusters is satisfactory compared with the full-scale solution, with minor discrepancies only in the tangential velocity of the red cluster. In terms of

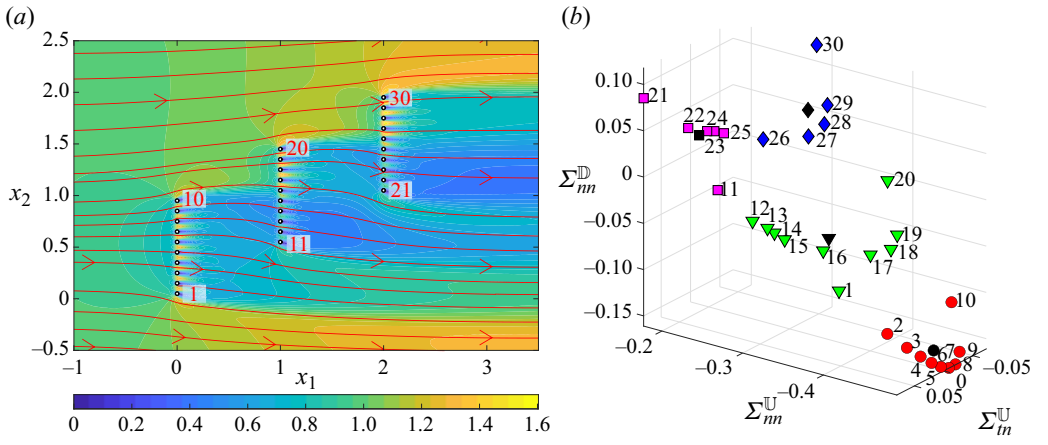

Figure 23. (*a*) Contours of velocity magnitude and streamlines (red) in the full-scale solution for $\alpha = 90°$, $\epsilon = 0.1$ and $Re_L = 500$. Each of the three identical membranes contains ten circular solid inclusions of porosity 0.7 and spacing ϵ. Inclusions 1, 11 and 21 are located in $(0, 0)$, $(L, 0.5L)$ and $(2L, L)$, respectively. The domain extent is $x_1 \in [-1.5L, 5.5L]$ and $y \in [-1.5L, 3.5L]$. No slip is imposed on the top and bottom sides of the domain, while $(u_1, u_2) = (1, 0)$ is imposed on the leftmost side and $\Sigma_{ij}n; j = 0$ on the rightmost side of the domain. Cells are numbered from bottom to top and left to right (red text). (*b*) A possible clustering choice for the cells on the membrane obtained using the MATLAB k-Means algorithm. Each cluster is visualized in a different marker and colour. Black markers represent the centroids of each cluster. Here, $\Sigma^{\mathbb{D}}_{in}$ is close to zero, thus it does not affect the results and it is hence not shown. Black numbers refer to corresponding cells in panel (*a*).

required computational resources, on a laptop with one INTEL i9-10900HK CPU (8 cores, 2.40 GHz) and 32 GB of RAM, a microscopic variable advection closure simulation has a run-time of up to 3 min, while a macroscopic simulation takes approximately 1 min. The clustering step proposed in this section has reduced the number of microscopic problems from 30 to 4 cases per iteration, which translates into a microscopic iteration step 7.5 times faster. In general, if we suppose that the number of iterations and the number of clusters at each iteration are $O(1)$, while the number of microscopic cases to run at each iteration without clustering is $O(1/\epsilon)$, then clustering makes the iterative procedure $O(1/\epsilon)$ times faster. For the cases proposed in this work, a few iterations were needed for convergence: for ϵRe_L of order 10, generally, 1−2 iterations are sufficient, while for ϵRe_L of order 100, we need 5–6 iterations.

Concerning the case proposed in figure 23, this case reaches a steady state in approximately 100 time units. In a laptop with one INTEL i9-10900HK CPU (8 cores, 2.40 GHz) and 32 GB of RAM, the full-scale simulation (∼270k degrees of freedom, kDOFs) has a runtime of approximately 310 s. The runtime of the macroscopic simulation sums up as follows: approximately 5 s for a single initial Stokes microscopic problem, 80 s for the initial variable advection microscopic problem (∼140 kDOFs), initialized with the Stokes solution, approximately 35 s for each of the following variable advection microscopic problems, initialized with the previous solution. A single macroscopic solution (∼55 kDOFs) takes approximately 10 s. The problem requires three iterations (initialization included) and can be accurately approximated with four clusters for the microscopic problems. The total runtime for the macroscopic simulation is $5\text{ s} + 80\text{s} + 2 \times 4 \times 35\text{ s} + 3 \times 10\text{ s} = 395\text{ s}$. In the present case and from a total runtime point of view, using the macroscopic model does not imply a substantial computational gain. However, we should consider that:

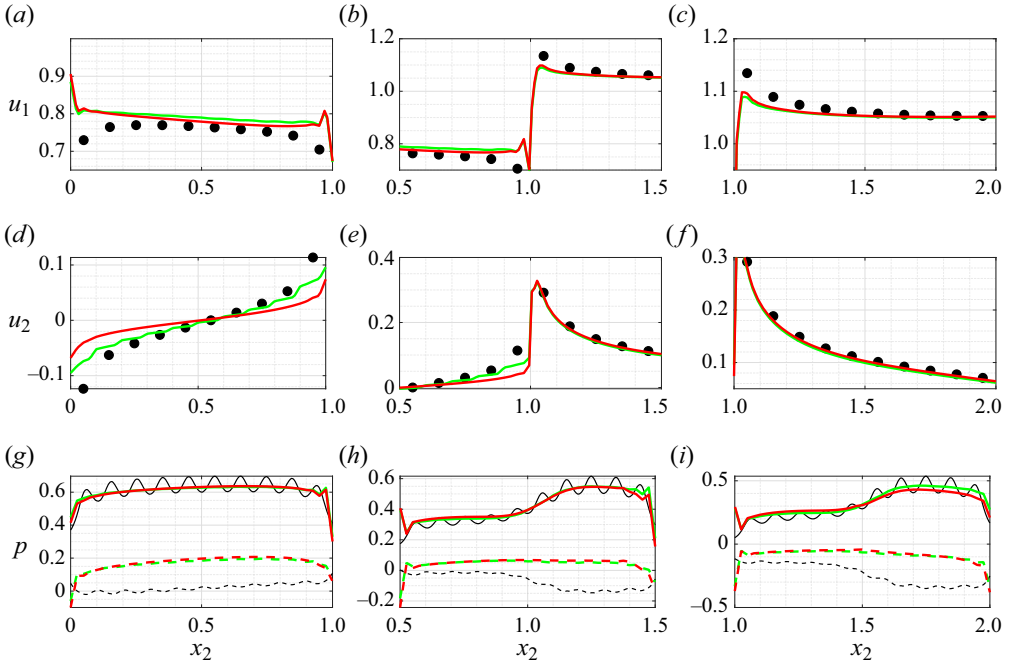

Figure 24. (*a–c*) Normal and (*d–f*) tangential velocity components on the centreline of each membrane. Black dots represent cell-averaged values of the full-scale solution, green lines represent the unclustered variable advection closure model and red lines are the clustered variable advection closure model. (*g–i*) Pressure values sampled at $\pm\epsilon/2$ from each centreline in the full-scale solution (full black line) and corresponding values for the unclustered variable advection closure model (green) and clustered variable advection closure (red) sampled on the corresponding sides of the fictitious interfaces. Panels (*a*,*d*,*g*) refer to the leftmost membrane, panels (*b*,*e*,*h*) to the central one and panels (*c*,*f*,*i*) to the rightmost membrane in figure 23(*a*).

(i) the macroscopic simulation is ϵ-insensitive, i.e. its computational cost does not depend on the ratio between the pore and the membrane scales, whereas the full-scale simulation depends mainly on ϵ, since it requires resolving all details of the microstructure;

(ii) in the macroscopic simulation, there are no mesh expansion-ratio-related problems, whereas it can be the case for the full-scale simulation, in particular, when ϵ is low or the microstructure has a non-trivial shape;

(iii) the RAM usage in the macroscopic case is reduced compared with the full-scale simulation since the iterative procedure splits the microscopic and macroscopic simulations;

(iv) most of the difference in runtime between the macroscopic and full-scale simulations stems from the microscopic coupling step. Creating a database of geometries and advective-velocity conditions or finding a surrogate model for them could further reduce the computational cost of the macroscopic simulation, making it of the order of the single macroscopic step in the coupling procedure.

These factors suggest that there is a gain in computational effort in using the present model when: (i) the scale separation is extreme (i.e. small ϵ); (ii) the details of the microstructure require a non-negligible effort in preparing the mesh; (iii) the advective velocities are close to some representative mean value; and (iv) the RAM usage is limited. An even more

significant gain is expected with surrogate models based on a large dataset of microscopic simulations.

6. Conclusion and perspectives

In this work, we developed a quasi-linear model to predict the solvent flow and diluted solute transport across thin permeable membranes in the case of non-negligible inertia at the pore scale. We exploited the separation of scales between the membrane and the pore size to decompose the mathematical problem into purely macroscopic equations and a microscopic problem which requires parametric inputs from the macro-scale stemming from the flow inertia at the pore scale. The presence of inertia therefore requires the approximation of the advective terms in the equations for the solvent flow and solute transport. An iterative procedure is employed to feed the microscopic problems with the macroscopic quantities included in the inertial terms within the Navier–Stokes and advection–diffusion equations. The macroscopic solution converges in an average sense to the fully resolved direct numerical simulations on the membrane and in the far-field.

Our work aims at extending the macroscopic, homogenized, description of filtration flows across permeable membranes towards practical applications when the Reynolds and Péclet numbers at the pore scale cannot be neglected. A relevant improvement in accuracy compared with the inertia-less version is found, for microscopic Reynolds number of order 10. In addition, preliminary faithful results can be obtained through machine learning clustering algorithms. This approach could offer a beneficial trade-off between efficiency and accuracy for large systems of industrial interest, such as filters or fuel cells (Cullen *et al.* 2021; Wang *et al.* 2023). In typical applications involving microfluidic circuits, flow inertia is either disregarded or considered a detrimental effect since it may affect the low-Reynolds-number hydrodynamic analytical predictions. However, our model establishes a specific relation between permeability properties and flow inertia. Hence, filtration properties can be finely tuned by selecting the flow rate within microfluidic channels, using the Reynolds and Péclet numbers as control parameters, and thus become a design parameter in addition to geometrical properties. As a matter of fact, for the same geometry, one can obtain a broad spectrum of filtration properties by simply changing the flow rate. Flow inertia thus becomes an opportunity to extend the working conditions of filtering systems.

This work could be extended in several ways. First, in the present form, the model cannot be applied to the case of macroscopic unsteady configuration triggered by pore-scale hydrodynamic instabilities (Nicolle & Eames 2011). To extend the model towards larger Reynolds numbers, space–time averages need to be introduced and data-aided physics-informed microscopic models are required to efficiently handle the micro–macro coupling. The quasi-linear iterative strategy developed in the present paper may open the door to the modelling of other, low-Re, nonlinear phenomena, such as the variation of viscosity with the solute concentration and osmotic or phoretic flows through semi-permeable structures, which typically present a strong nonlinear coupling between the solvent velocity and the solute concentration (Marbach, Yoshida & Bocquet 2017).

Acknowledgements. The authors are profoundly grateful to Prof. F. Gallaire for his assistance and, in particular, for the insightful discussions concerning the treatment of the nonlinearities in the microscopic problem.

Funding. This work was supported by the Swiss National Science Foundation (grant no. *PZ*00*P*2_193180).

Declaration of interests. The authors report no conflict of interest.

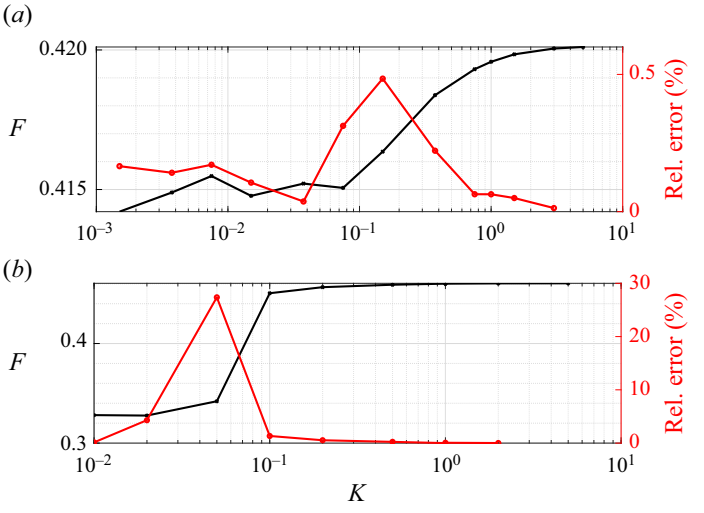

Figure 25. Force magnitude F (black) acting on (*a*) $\mathbb{C}$ in the macroscopic simulation and (*b*) on the solid boundary $\partial\mathbb{M}$ in the full-scale simulation and relative error between two consequent values of F (red) as a function of K for $Re_L = 500$, $\alpha = 90^\circ$, $\epsilon = 0.1$ and circular solid inclusions of porosity 0.7.

Code availability. The source code, along with some examples, is available on GitHub at this link.

Author ORCIDs.
K. Wittkowski https://orcid.org/0000-0001-5896-8266;
P.G. Ledda https://orcid.org/0000-0003-4435-8613;
G.A. Zampogna https://orcid.org/0000-0001-7570-9135.

Appendix A. Computational details

The microscopic and macroscopic equations and the full-scale solution presented in § 4 have been solved numerically using the finite-element solver COMSOL Multiphysics 6.0. The coupling between the microscopic and the macroscopic problems is automated thanks to the MATLAB Livelink extension. The spatial convergence of the mesh has been tested for each model and flow configuration. The same criterion has been used for the microscopic calculations. All simulations are performed using a Taylor–Hood P2-P1 scheme for coupling velocity and pressure and a P2 scheme for the solute concentration. The deriving linear systems are solved using MUMPS and a time marching procedure is exploited to find the stationary solution. We present hereafter the results of the convergence study for $\epsilon = 0.1$, $Re_L = 500$, $\alpha = 90^\circ$ and circular inclusions with porosity 0.7 for the macroscopic and full-scale simulations. We start with a mesh whose typical size is:

(i) $0.01L$ on the macroscopic interface and $0.045L$ far from it for the macroscopic problem (corresponding to $K = 1$ in figure 25*a*);
(ii) $0.0015L$ on the solid boundary and $0.05L$ far from it for the full-scale problem (corresponding to $K = 1$ in figure 25*b*);
(iii) 0.04ℓ near the solid inclusion and 0.5ℓ far from them for the microscopic problems (corresponding to $K = 1$ in figure 1),

and explore a range of K values to verify that the results are mesh-independent, where K is a parameter dividing the initial mesh sizing for each simulation. We consider the mesh converged when the force magnitude $F = \| \int_{\mathbb{C}} \Sigma_{ij} n_j \, \mathrm{d}S \|$ applied by the fluid on the

https://doi.org/10.1017/jfm.2024.987 Published online by Cambridge University Press

K	$\bar{M}_{nn}$	$\bar{M}_{nt}$	$\bar{M}_{tn}$	$\bar{M}_{tt}$	$\bar{N}_{nn}$	$\bar{N}_{nt}$	$\bar{N}_{tn}$	$\bar{N}_{tt}$
100	1.453×10^{-2}	4.007×10^{-5}	5.045×10^{-15}	-4.655×10^{-15}	-1.453×10^{-2}	-4.007×10^{-5}	-2.208×10^{-6}	-3.027×10^{-3}
50	1.453×10^{-2}	4.001×10^{-5}	2.402×10^{-13}	-4.656×10^{-14}	-1.453×10^{-2}	-4.001×10^{-5}	-2.322×10^{-6}	-3.030×10^{-3}
10	1.454×10^{-2}	5.223×10^{-5}	-6.720×10^{-4}	-4.719×10^{-5}	-1.454×10^{-2}	-5.223×10^{-5}	2.318×10^{-4}	-3.012×10^{-3}
5	1.454×10^{-2}	4.994×10^{-5}	-5.528×10^{-4}	-3.025×10^{-5}	-1.454×10^{-2}	-4.994×10^{-5}	1.902×10^{-4}	-3.017×10^{-3}
2	1.454×10^{-2}	5.008×10^{-5}	-5.637×10^{-4}	-2.807×10^{-5}	-1.454×10^{-2}	-5.008×10^{-5}	1.939×10^{-4}	-3.018×10^{-3}
1	1.294×10^{-2}	1.156×10^{-3}	-4.071×10^{-2}	-4.199×10^{-3}	-1.294×10^{-2}	-1.156×10^{-3}	1.196×10^{-2}	-1.900×10^{-3}

Table 1. Averaged values of M_{ij} as a function of the mesh factor K for a microscopic problem with variable advection computed around a circular solid inclusion of porosity 0.7 for $\check{\Sigma}_{ij}^{\mathbb{U}} = 10^4$ and $\check{\Sigma}_{ij}^{\mathbb{D}} = 0$. Only the values of $\bar{M}_{nn}, \bar{N}_{nn}$ and $\bar{N}_{tt}$ are considered for the mesh convergence study since the other components have negligible values at convergence ($K \geq 10$).

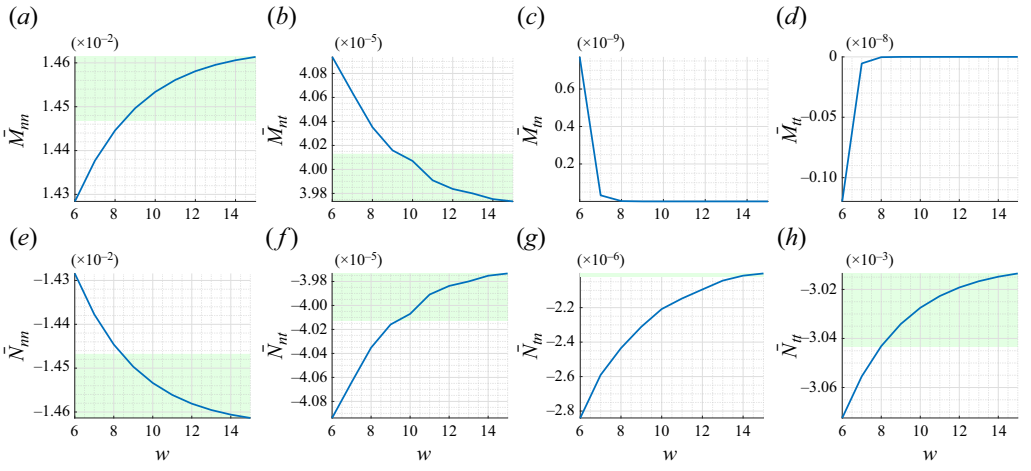

Figure 26. Microscopic tensors average values as a function of the domain amplitude w [ℓ]. The green shaded zone corresponds to a range of ± 1 % about the tensor value obtained at maximum domain amplitude.

fictitious interface $\mathbb{C}$ in the macroscopic simulation and on $\partial\mathbb{M}$ in the full-scale simulation reaches an asymptotic value and the relative error between two F values sampled at two subsequent values of K is less than 0.2 %. The converged macroscopic mesh has 91 304 elements and the full-scale one has 237 900, both corresponding to $K = 1$ (cf. figure 25). The parameters of the microscopic case are $\check{\Sigma}_{ij}^{\mathbb{U}} n_j = 10^4$ and $\check{\Sigma}_{ij}^{\mathbb{D}} n_j = 0$. We consider the mesh converged when the relative difference between the non-zero values of $\bar{M}_{ij}$, $\bar{N}_{ij}$ is less than 1 % for two subsequent values of K. The final mesh contains 12 780 elements, corresponding to $K = 10$ in table 1. We also tested the convergence of the microscopic problems concerning changes in the domain width in the normal direction, w. We present a typical convergence study for $\check{\Sigma}_{nn}^{\mathbb{U}} = \check{\Sigma}_{tn}^{\mathbb{U}} = 10^4$ and $\check{\Sigma}_{nn}^{\mathbb{D}} = \check{\Sigma}_{tn}^{\mathbb{D}} = 0$ in figure 26. The green shaded zone corresponds to a range of ± 1 % about the value at maximum amplitude w of each tensor component and is used as a threshold for convergence. Only the relevant tensor components $\bar{M}_{nn}$, $\bar{M}_{nt}$, $\bar{N}_{nn}$, $\bar{N}_{nt}$ and $\bar{N}_{tt}$ have been used to test the convergence of the tensors with respect to the domain width. A domain of length 9ℓ represents a good trade-off between accuracy and computational cost.

Appendix B. Further variable advection closure maps

Figures 27–31 present further 2-D sub-manifolds of the 4-D manifold of $\bar{M}_{ij}$ and $\bar{N}_{ij}$ values found by solving the variable advection closure microscopic problem (2.21).

Appendix C. Flow inside a channel obstructed by a membrane

Zampogna & Gallaire (2020) proposed several macroscopic validation cases, among which is a 2-D channel obstructed by the presence of a membrane on its full section. We consider a similar test case, a 2-D channel of dimensions $7L \times 1L$, obstructed by a porous membrane constituted by 10 circular solid inclusions of porosity $\theta = 0.7$. Figure 32 shows the corresponding pressure fields and streamlines in (a) the full-scale, (b) macroscopic obtained using Stokes approximation and (c) macroscopic obtained with the variable advection closure cases. Panels (d,e) show the average velocity components sampled along $\mathbb{C}$. The problem is dominated by mass conservation since the flow is forced to cross the

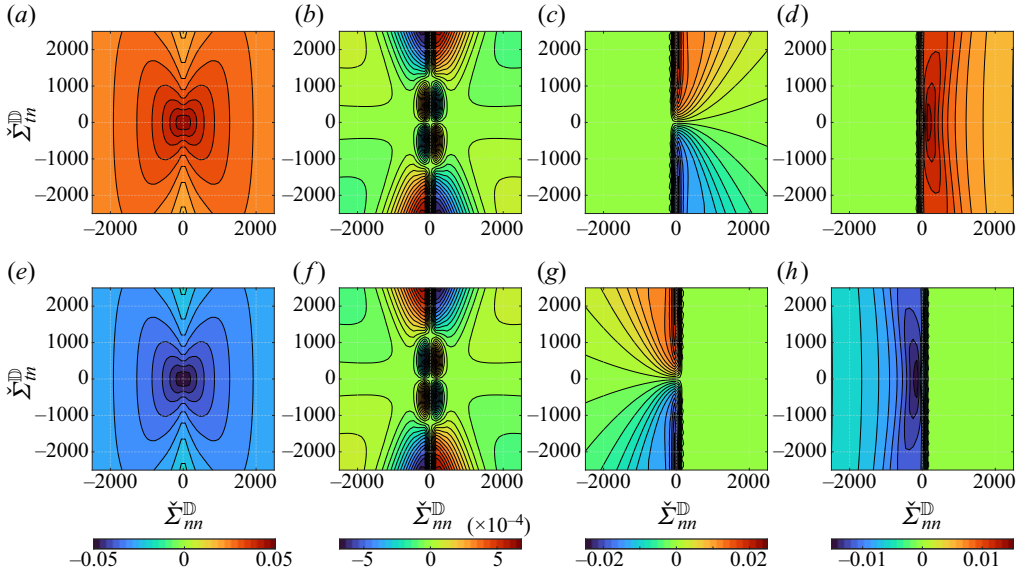

Figure 27. Average tensor values (*a*) $\bar{M}_{nn}$, (*b*) $\bar{M}_{nt}$, (*c*) $\bar{M}_{tn}$, (*d*) $\bar{M}_{tt}$, (*e*) $\bar{N}_{nn}$, (*f*) $\bar{N}_{nt}$, (*g*) $\bar{N}_{tn}$, (*h*) $\bar{N}_{tt}$ varying $\check{\Sigma}^{\mathbb{D}}_{nn}$ and $\check{\Sigma}^{\mathbb{D}}_{tn}$, while $\check{\Sigma}^{\mathbb{U}}_{nn} = \check{\Sigma}^{\mathbb{U}}_{tn} = 0$.

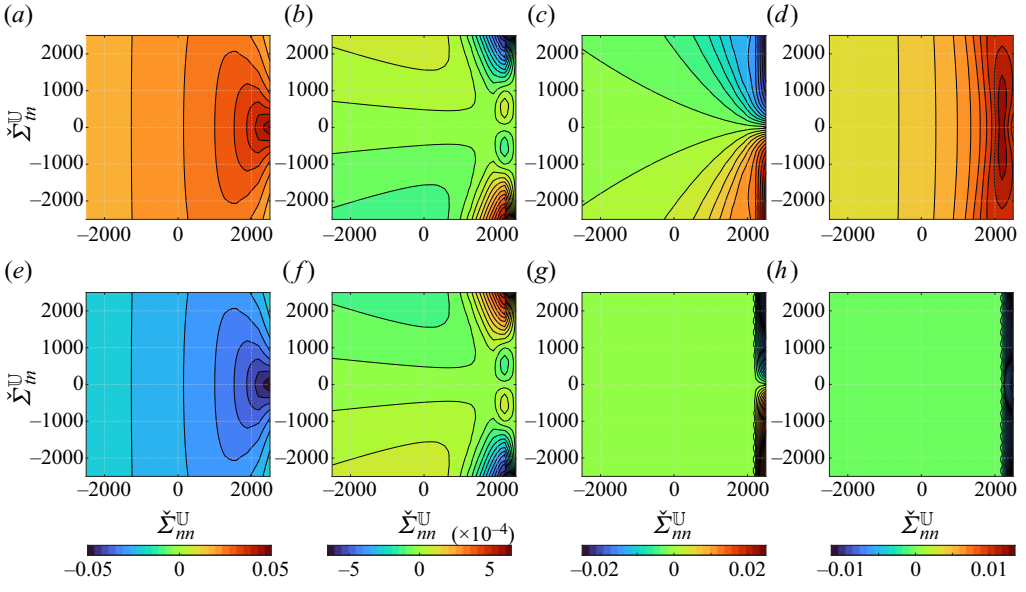

Figure 28. Average tensor values (*a*) $\bar{M}_{nn}$, (*b*) $\bar{M}_{nt}$, (*c*) $\bar{M}_{tn}$, (*d*) $\bar{M}_{tt}$, (*e*) $\bar{N}_{nn}$, (*f*) $\bar{N}_{nt}$, (*g*) $\bar{N}_{tn}$, (*h*) $\bar{N}_{tt}$ varying $\check{\Sigma}^{\mathbb{U}}_{nn} = \epsilon^2 Re_L^2 \Sigma^{\mathbb{U}}_{nn}$ and $\check{\Sigma}^{\mathbb{U}}_{tn}$, while $\check{\Sigma}^{\mathbb{D}}_{nn} = 2500$ and $\check{\Sigma}^{\mathbb{D}}_{tn} = 0$.

membrane. The velocity on the membrane using the Stokes and the variable advection closure models is predicted with similar accuracy. However, the pressure fields show major differences upstream of the membrane, confirming the superior accuracy of the variable advection closure model with respect to the Stokes model.

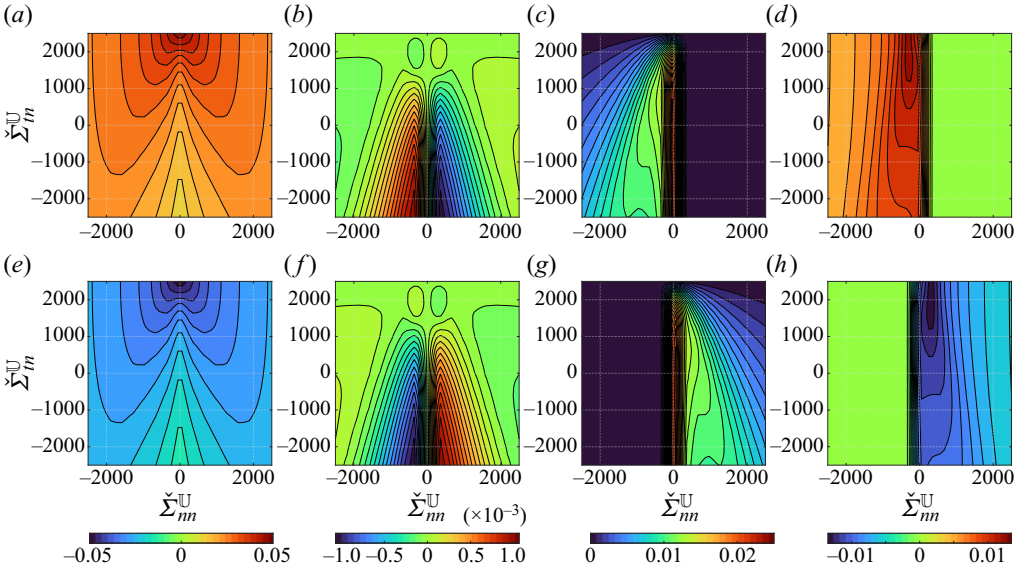

Figure 29. Average tensor values (*a*) $\bar{M}_{nn}$, (*b*) $\bar{M}_{nt}$, (*c*) $\bar{M}_{tn}$, (*d*) $\bar{M}_{tt}$, (*e*) $\bar{N}_{nn}$, (*f*) $\bar{N}_{nt}$, (*g*) $\bar{N}_{tn}$, (*h*) $\bar{N}_{tt}$ varying $\check{\Sigma}^{\mathbb{U}}_{nn} = \epsilon^2 Re_L^2 \Sigma^{\mathbb{U}}_{nn}$ and $\check{\Sigma}^{\mathbb{U}}_{tn}$, while $\check{\Sigma}^{\mathbb{D}}_{nn} = 0$ and $\check{\Sigma}^{\mathbb{D}}_{tn} = 2500$.

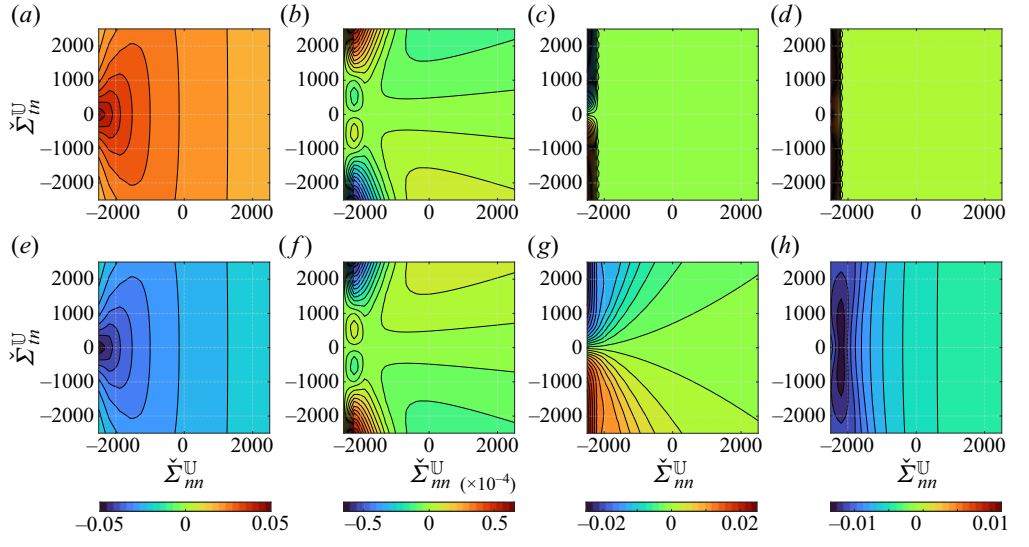

Figure 30. Average tensor values (*a*) $\bar{M}_{nn}$, (*b*) $\bar{M}_{nt}$, (*c*) $\bar{M}_{tn}$, (*d*) $\bar{M}_{tt}$, (*e*) $\bar{N}_{nn}$, (*f*) $\bar{N}_{nt}$, (*g*) $\bar{N}_{tn}$, (*h*) $\bar{N}_{tt}$ varying $\check{\Sigma}^{\mathbb{U}}_{nn} = \epsilon^2 Re_L^2 \Sigma^{\mathbb{U}}_{nn}$ and $\check{\Sigma}^{\mathbb{U}}_{tn}$, while $\check{\Sigma}^{\mathbb{D}}_{nn} = -2500$ and $\check{\Sigma}^{\mathbb{D}}_{tn} = 0$.

Appendix D. Comparison between microscopic constant advection closure solutions and experimental data

In § 3.1, we observed that the permeability $\bar{M}_{nn}$ decreases as the flow inertia within the pore increases. In this section, we compare the theoretical model of Jensen *et al.* (2014*b*) and the experimental results of Johansen (1930) with the constant advection closure model prediction. Indeed, the latter allows for a direct comparison since the flow inertia is

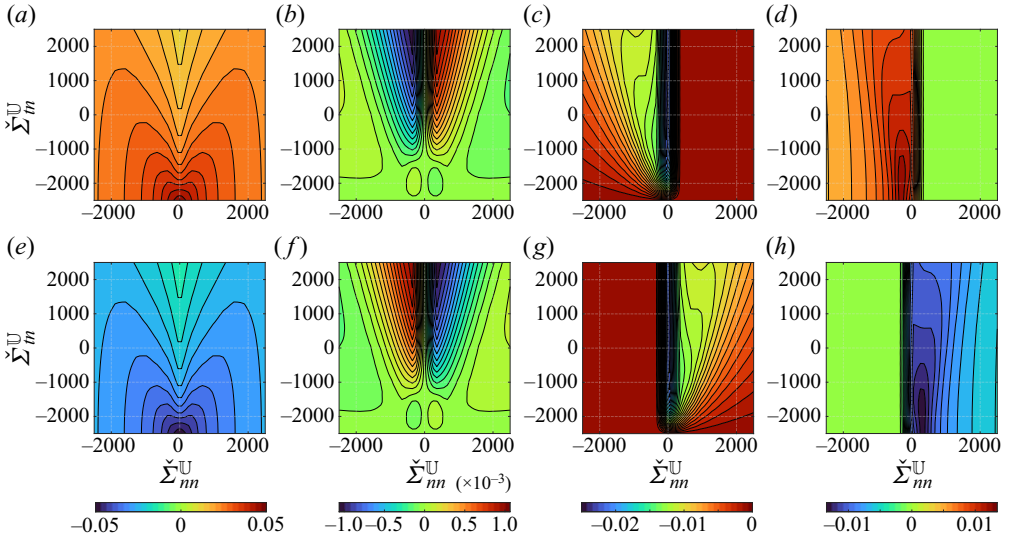

Figure 31. Average tensor values (*a*) $\bar{M}_{nn}$, (*b*) $\bar{M}_{nt}$, (*c*) $\bar{M}_{tn}$, (*d*) $\bar{M}_{tt}$, (*e*) $\bar{N}_{nn}$, (*f*) $\bar{N}_{nt}$, (*g*) $\bar{N}_{tn}$, (*h*) $\bar{N}_{tt}$ varying $\check{\Sigma}^{\mathbb{U}}_{nn} = \epsilon^2 Re_L^2 \Sigma^{\mathbb{U}}_{nn}$ and $\check{\Sigma}^{\mathbb{U}}_{tn}$, while $\check{\Sigma}^{\mathbb{D}}_{nn} = 0$ and $\check{\Sigma}^{\mathbb{D}}_{tn} = -2500$.

expressed in terms of average velocity (or microscopic Reynolds number) across the pore. Starting from the Stokes flow solution across a circular pore, Jensen *et al.* (2014*b*) proposed the following empirical model for the normal flow of a viscous fluid across a periodic, thin, porous membrane, in the presence of inertia:

$$\frac{\hat{q}}{\Delta\hat{p}} = \frac{\hat{a}^3}{3\mu\left[\dfrac{8}{3\pi}\dfrac{\hat{t}}{\hat{a}} - G\left(\dfrac{\hat{a}}{\ell}\right)^3 + \dfrac{\phi(Re_{pore})}{3}\right]}, \tag{D1}$$

where $\hat{q}$ is the pore flow rate, $\Delta\hat{p}$ is the pressure drop across the membrane, $\hat{t}$ is the membrane thickness, $\hat{a}$ is the pore radius, ℓ is the pore array centre-to-centre distance and $\phi = 3 + (Re_{pore} - Re^T_{pore})/\pi$ is a term representing the inertial effects. The term Re^T_{pore} is a parameter representing the transition between the inertia-less and inertial regime in the pore: Jensen *et al.* (2014*b*) obtained a value of $Re^T_{pore} = 4$ by fitting from experimental data. In addition, G is a coefficient that represents the effect of the pore arrangement on the membrane (for a square array of pores, the authors suggest $G = 1.9$) and $Re_{pore} = \rho\hat{u}a/\mu$ ($\hat{u}$ is the pore average velocity). Non-dimensionalizing (D1) with the inner scales, we get

$$\frac{q}{\Delta p} = \frac{a^3}{3\left[\dfrac{8}{3\pi}\dfrac{t}{a} - 1.9(a)^3 + \dfrac{\phi(Re_{pore})}{3}\right]}. \tag{D2}$$

As a matter of fact, $q/\Delta p = a^3/\phi(Re_{pore})$ is the classic Darcy permeability term which, in our work, corresponds to $\bar{M}_{nn}$. The parameters for the constant advection closure model (2.20) in this case are $Re_{pore} = (a)Re_\ell$ and $U = (1, 0, 0)$ (pure normal advection). The considered pore has a non-dimensional radius $a = 0.25$ and non-dimensional thickness $t = a/2$ (see geometry in figure 33*a*). A comparison between the model of Jensen *et al.* (2014*b*) and our result is reported in figure 33(*a*) for a square array of pores in terms

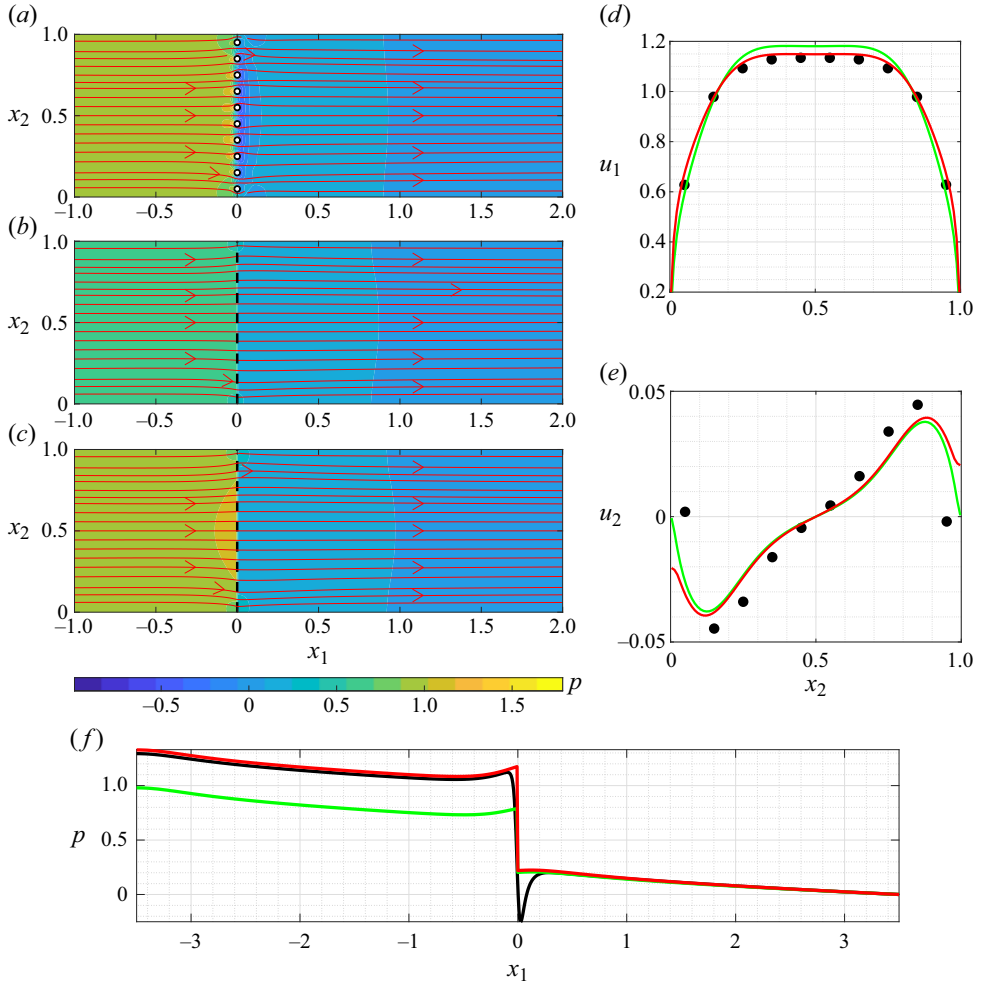

Figure 32. Flow across a membrane obstructing a 2-D channel at $Re_L = 400$. Pressure contours and streamlines for (*a*) the full-scale, (*b*) macroscopic with Stokes approximation and (*c*) macroscopic with variable advection closure models. (*d*) Horizontal and (*e*) vertical average velocity components on the membrane: full-scale (black), macroscopic with Stokes (green) and macroscopic with the variable advection closure model (red). (*f*) Pressure sampled on a line crossing the whole domain at $x_2 = 0.5$: full-scale (black), macroscopic with Stokes (green) and macroscopic with the variable advection closure model (red). The original domain is $7L \times 1L$ wide, but here we focus on the flow near the membrane.

of permeability. Additionally, we isolate the effect of inertia by considering $\phi(Re_{pore}) - \phi(Re_{pore} = 0)$ in figure 33(*b*). To compute this term from $\bar{M}_{nn}$ and without any fitting coefficient, we start from (21) of Jensen *et al.* (2014*b*) and non-dimensionalize, obtaining

$$\phi^{CA}(Re_{pore}) = \frac{a^3}{\bar{M}_{nn}(Re_{pore})}. \tag{D3}$$

Jensen *et al.* (2014*b*) suggested that the effect of inertia ϕ in a pure normal flow can be modelled as a linear function of the pore Reynolds number of slope $1/\pi$ in the inertial regime (i.e. $Re_{pore} > Re^T_{pore} = 4$), which well agrees with our predictions. Furthermore, the comparison with the experimental data of Johansen (1930) in figure 33(*b*) depicts a

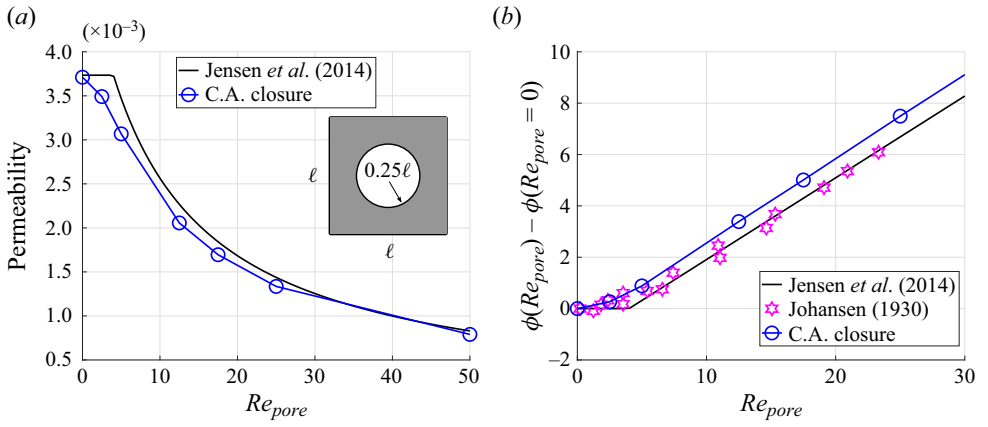

Figure 33. (*a*) Permeability coefficient and (*b*) inertial coefficient ϕ as a function of the pore Reynolds number Re_{pore}. We compare the theoretical prediction obtained using (D2) (black), the constant advection closure model (blue) and the experimental data of Johansen (1930) (magenta). The inset in panel (*a*) shows the pore geometry.

good agreement also in terms of actual values of ϕ. We conclude by noting that our model is also able to capture the smooth transition from the Stokes regime to the inertial one.

References

Arthur, D. & Vassilvitskii, S. 2007 K-means++: the advantages of careful seeding. In *Proceedings of the Eighteenth Annual ACM-SIAM Symposium on Discrete Algorithms*, pp. 1027–1035. Society for Industrial and Applied Mathematics.

Bishop, C.M. 2006 *Pattern Recognition and Machine Learning*, pp. 423–450. Springer.

Bottaro, A. 2019 Flow over natural or engineered surfaces: an adjoint homogenization perspective. *J. Fluid Mech.* **877**, P1.

Bourgeat, A. & Marusic-Paloka, E. 1998 Mathematical modelling of a non-Newtonian viscous flow through a thin filter. *C. R. Acad. Sci. Ser.* I *Math.* **327**, 607–612.

Catarino, S.O., Rodrigues, R.O., Pinho, D., Miranda, J.M., Minas, G. & Lima, R. 2019 Blood cells separation and sorting techniques of passive microfluidic devices: from fabrication to applications. *Micromachines* **10** (9), 593.

Conca, C. 1987 Etude d'un fluide traversant une paroi perforee I. Comportement limite loin de la paroi. *J. Math. Pures Appl.* **66**, 45–69.

Cullen, D.A., Neyerlin, K.C., Ahluwalia, R.K., Mukundan, R., More, K.L., Borup, R.L., Weber, A.Z., Myers, D.J. & Kusoglu, A. 2021 New roads and challenges for fuel cells in heavy-duty transportation. *Nat. Energy* **6** (5), 462–474.

Cummins, C., Seale, M., Macente, A., Certini, D., Mastropaolo, E., Viola, I.M. & Nakayama, N. 2018 A separated vortex ring underlies the flight of the dandelion. *Nature* **562** (7727), 414–418.

Dagan, G. 1987 Theory of solute transport by groundwater. *Annu. Rev. Fluid Mech.* **19** (1), 183–213.

Darcy, H. 1856 *Les fontaines publiques de la ville de Dijon: exposition et application des principes a suivre et des formules a employer dans les questions de distribution d'eau*. Victor Dalmont.

Einstein, A. 1906 Eine neue bestimmung der moleküldimensionen. *Ann. Phys.* **324** (2), 289–306.

Falcucci, G., Amati, G., Bella, G., Facci, A.L., Krastev, V.K., Polverino, G., Succi, S. & Porfiri, M. 2024 Adapting to the abyss: passive ventilation in the deep-sea glass sponge *Euplectella aspergillum*. *Phys. Rev. Lett.* **132**, 208402.

Falcucci, G., Amati, G., Fanelli, P., Krastev, V.K., Polverino, G., Porfiri, M. & Succi, S. 2021 Extreme flow simulations reveal skeletal adaptations of deep-sea sponges. *Nature* **595** (7868), 537–541.

Geback, T. & Heintz, A. 2019 A pore scale model for osmotic flow: homogenization and lattice Boltzmann simulations. *Transp. Porous Media* **126**, 161–176.

Goldsack, D. & Franchetto, R. 2011 The viscosity of concentrated electrolyte solutions. II. Temperature dependence. *Can. J. Chem.* **55**, 1062–1072.

Hornung, U. 1997 *Homogenization and Porous Media*. Springer.

ICARDI, M., BOCCARDO, G., MARCHISIO, D.L., TOSCO, T. & SETHI, R. 2014 Pore-scale simulation of fluid flow and solute dispersion in three-dimensional porous media. *Phys. Rev.* E **90**, 013032.

JENSEN, K.H., ANDRÉ, X.C.N. & STONE, H.A. 2014*a* Flow rate through microfilters: influence of the pore size distribution, hydrodynamic interactions, wall slip and inertia. *Phys. Fluids* **26**, 052004.

JENSEN, K.H., VALENTE, A.X.C.N. & STONE, H.A. 2014*b* Flow rate through microfilters: influence of the pore size distribution, hydrodynamic interactions, wall slip, and inertia. *Phys. Fluids* **26** (5), 052004.

JOHANSEN, F.C. 1930 Flow through pipe orifices at low Reynolds numbers. *Proc. R. Soc. Lond.* A *Math. Phys. Sci.* **126** (801), 231–245.

LABBÉ, R. & DUPRAT, C. 2019 Capturing aerosol droplets with fibers. *Soft Matt.* **15** (35), 6946–6951.

LĀCIS, U., SUDHAKAR, Y., PASCHE, S. & BAGHERI, S. 2020 Transfer of mass and momentum at rough and porous surfaces. *J. Fluid Mech.* **884**, A21.

LEDDA, P.G., BOUJO, E., CAMARRI, S., GALLAIRE, F. & ZAMPOGNA, G.A. 2021 Homogenization-based design of microstructured membranes: wake flows past permeable shells. *J. Fluid Mech.* **927**, A31.

LEDDA, P.G., SICONOLFI, L., VIOLA, F., CAMARRI, S. & GALLAIRE, F. 2019 Flow dynamics of a dandelion pappus: A linear stability approach. *Phys. Rev. Fluids* **4**, 071901.

LUMINARI, N., AIRIAU, C. & BOTTARO, A. 2018 Effects of porosity and inertia on the apparent permeability tensor in fibrous media. *Intl J. Multiphase Flow* **106**, 60–74.

MARBACH, S., YOSHIDA, H. & BOCQUET, L. 2017 Osmotic and diffusio-osmotic flow generation at high solute concentration. I. Mechanical approaches. *J. Chem. Phys.* **146** (19), 194701.

MONCUQUET, A., MITRANESCU, A., MARCHAND, O.C., RAMANANARIVO, S. & DUPRAT, C. 2022 Collecting fog with vertical fibres: combined laboratory and in-situ study. *Atmos. Res.* **277**, 106312.

NICOLLE, A. & EAMES, I. 2011 Numerical study of flow through and around a circular array of cylinders. *J. Fluid Mech.* **679**, 1–31.

PARK, K.-C., CHHATRE, S.S., SRINIVASAN, S., COHEN, R.E. & MCKINLEY, G.H. 2013 Optimal design of permeable fiber network structures for fog harvesting. *Langmuir* **29** (43), 13269–13277.

QUARTERONI, A. 2017 *Domain Decomposition Methods*, pp. 555–612. Springer International Publishing.

ROYER, P. 2019 Advection–diffusion in porous media with low scale separation: modelling via higher-order asymptotic homogenisation. *Transp. Porous Media* **128** (2), 511–551.

SÁNCHEZ-VARGAS, J., VALDÉS-PARADA, F.J., TRUJILLO-ROLDÁN, M.A. & LASSEUX, D. 2023 Macroscopic model for generalised Newtonian inertial two-phase flow in porous media. *J. Fluid Mech.* **970**, A19.

STROOCK, A.D., DERTINGER, S.K.W., AJDARI, A., MEZIĆ, I., STONE, H.A. & WHITESIDES, G.M. 2002 Chaotic mixer for microchannels. *Science* **295** (5555), 647–651.

SURESH, P.V. & JAYANTI, S. 2016 Péclet number analysis of cross-flow in porous gas diffusion layer of polymer electrolyte membrane fuel cell (PEMFC). *Environ. Sci. Pollut. Res.* **23** (20), 20120–20130.

TIBSHIRANI, R., WALTHER, G. & HASTIE, T. 2001 Estimating the number of clusters in a data set via the gap statistic. *J. R. Stat. Soc.* B *(Stat. Methodol.)* **63** (2), 411–423.

TIO, K.-K. & SADHAL, S.S. 1994 Boundary conditions for stokes flows near a porous membrane. *Appl. Sci. Res.* **52** (1), 1–20.

TRIPATHI, S., BALA VARUN KUMAR, Y.V., PRABHAKAR, A., JOSHI, S.S. & AGRAWAL, A. 2015 Passive blood plasma separation at the microscale: a review of design principles and microdevices. *J. Micromech. Microeng.* **25** (8), 083001.

VALDÉS-PARADA, F.J. & LASSEUX, D. 2021 Flow near porous media boundaries including inertia and slip: a one-domain approach. *Phys. Fluids* **33** (7), 073612.

VERKMAN, A.S. & MITRA, A.K. 2000 Structure and function of aquaporin water channels. *Am. J. Physiol.-Renal Physiol.* **278** (1), F13–F28.

WANG, Y.D., *et al.* 2023 Large-scale physically accurate modelling of real proton exchange membrane fuel cell with deep learning. *Nat. Commun.* **14** (1), 745.

WHITAKER, S. 1996 The Forchheimer equation: a theoretical development. *Transp. Porous Media* **25** (1), 27–61.

YANG, X., YANG, J.M., TAI, Y.-C. & HO, C.-M. 1999 Micromachined membrane particle filters. *Sensors Actuators* A*: Phys.* **73** (1), 184–191.

ZAMPOGNA, G.A. & GALLAIRE, F. 2020 Effective stress jump across membranes. *J. Fluid Mech.* **892**, A9.

ZAMPOGNA, G.A., LEDDA, P.G. & GALLAIRE, F. 2022 Transport across thin membranes: effective solute flux jump. *Phys. Fluids* **34** (8), 083113.

ZAMPOGNA, G.A., MAGNAUDET, J. & BOTTARO, A. 2019 Generalized slip condition over rough surfaces. *J. Fluid Mech.* **858**, 407–436.

ZAMPOGNA, G.A., PLUVINAGE, F., KOURTA, A. & BOTTARO, A. 2016 Instability of canopy flows. *Water Resour. Res.* **52** (7), 5421–5432.